Time Dependent Coupled Channels Approaches to Nuclear Collisions

Emlyn S. Graham

A thesis submitted for the degree of

Bachelor of Science with Honours in Physics at

The Australian National University

October, 2019

Declaration

This thesis is an account of research undertaken between February and October of 2019 at the Department of Nuclear Physics, Research School of Physics, The Australian National University, Canberra, Australia.

Except where acknowledged in the customary manner, the material presented in this thesis is, to the best of my knowledge, original and has not been submitted in whole or part for a degree in any university.

Emlyn S. Graham

October, 2019

Acknowledgements

I acknowledge the Ngunnawal and Ngambri people, upon whose land I conducted this work. I also acknowledge the traditional owners of other lands throughout Australia, and pay my respects to their elders past, present and emerging.

I would like to thank a great number of people for their support this year, and over my long educational career. First, thanks must go to my supervisor Ed. You have been the best combination of friendly and forceful, hands-on and hands-off, and have taught me a lot about how to do real research. My thanks also go to everyone else in the School of Physics, particularly Wiktoria and Nathan for their company on regular trips to re-caffeinate, and Tim and Dan for their company on several late nights.

My unconditional love goes to my parents, who inspired in me an appreciation for learning from a young age, and provided me the opportunities that made me the person I am today. Thank you. And finally Lucinda, who was there beside me every step of the way, making every day a better one. I'm looking forward to what the future holds.

Abstract

It is an exciting time to study nuclear fusion, as we progress ever closer to the 'island of stability' of long-lived superheavy elements. However, we do not fully understand the way that dissipative processes, for example the population of highly excited states of reactants, influence fusion. Current static coupled channels models do not allow for an explicit description of the dissipative processes, and as a result measured fusion cross sections for heavy element production are significantly overestimated. Static coupled channels also includes fusion as a non-physical irreversible process, without describing the complex dissipative processes that are inherent to fusion. Time-dependent coupled channels is a promising approach to include dissipative effects back into macroscopic fusion reaction computations which could predict fusion hindrance at above barrier energies, and allow for the physical description of fusion as dissipation. In this thesis I detail methods of including time-dependence in coupled channels by solving the time-dependent Schrödinger equation. I outline several ways this can be done, and describe the split step Fourier method as I implemented it in the C++ library Quantum Toolbox. The effectiveness of this implementation was rigorously tested for sources of error, and verified against analytic and coupled channels results for tunnelling and coupling respectively. Finally, the time-dependent approach was applied to the problems of dissipation before and during tunnelling. Early results indicate that a coupling forward of the barrier produces the coupling to match experimental outcomes, and is likely the source of above barrier suppression of fusion. Tests of coupling-induced wavefunction trapping inside the barrier suggest the technique could be used to compute fusion without the need for artificial absorption.

Contents

Introduction

Nuclear fusion is one of the most important quantum mechanical processes in the universe. It is through fusion that stars shine, allowing life to exist on earth [1]. It can be destructive if harnessed in a weapon, but will likely power all of human civilisation in the future. In the context of physics it is still not fully understood, a testing ground for experimental equipment and theories of many-body quantum dynamics. These aspects converge in the pursuit of new superheavy elements and the theoretical "island of stability", as yet unknown stable elements with around 112 protons. Fundamentally, fusion is a rapid dissipative process, converting the (often large) relative kinetic energy of the collision into a multitude of nucleonic excitations, in less than 10^{-2} seconds.

Quantum effects are extremely important in fusion. Classically, nuclei require enough energy to overcome the potential energy "barrier'âĂŹ to fuse. Tunnelling significantly changes rates of nuclear fusion, in particular allowing for fusion at energies below this fusion barrier. Furthermore, nuclei have a plurality of possible internal states; their component nucleons can be individually excited, can vibrate collectively, and neutrons can be exchanged between the interacting nuclei. Excitation of these states during the interac-
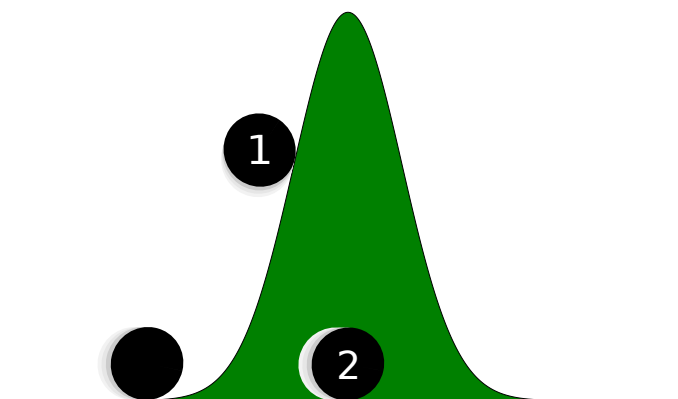
Figure 1.1: An illustration of quantum tunnelling. In most cases the quantum object will follow the path of 1, but in some cases it may tunnel, following the path of 2 and measured on the other side.

tions of nuclei can have a profound effect on tunnelling, enhancing probabilities by many orders of magnitude [2]. These couplings are critical to our understanding of heavy ion fusion. The coupling acts to lower the effective barrier to fusion, making it easier to fuse at low energy.

Coupled channels models, which were traditionally used to describe the scattering of nuclei, have had some success in describing nuclear fusion [3]. Given the Hamiltonian description of the interacting nuclei, coupled Schrödinger equations can be solved numerically to calculate the rate of fusion and cross sections. This has become the de facto approach internationally, with implementations such as CCFULL successfully matching many experimental results [4].

Despite the success of coupled channels, in recently years evidence has been mounting that the currently coupled channels approach insufficiently describes fusion and the processes that lead to it. This scepticism has been driven by the systematic overestimation of experimental results by coupled channels at energies above the fusion barrier [5]. Underlying this overestimation are several possible problems caused by the fundamentally dissipative nature of fusion which is neglected in coupled channels.

Firstly, static coupled channels models have no explicit description of the dissipative processes that lead to fusion. Indeed, fusion is implemented with an artificial boundary condition or absorbing potential placed inside the barrier. In a static picture, this is the only way to ensure the system remains fused. Secondly, dissipation exhibits itself before fusion occurs, reducing the rate of fusion, but is poorly understood. It has been proposed that the transfer of neutrons between nuclei may be the cause of this, dynamically altering the height of the fusion barrier. These processes are routinely neglected in static coupled channels calculations. All of these points lead to one conclusion; there is need for a time-dependent model of fusion. Coupled channels models are very successful, and so introducing time-dependence to these is the clearest path. This leads to two key questions:

- What can time dependent methods tell us about dissipation prior to fusion?

- Can we simulate fusion using time-dependent coupled channels without the need for artificial boundary conditions?

Addressing these questions will render further benefits over the traditional coupled channels. Types of scattering and fusion are more naturally identified in a time-dependent model, as they are well distinguished by their time of occurrence. Time dependence also

allows for more natural descriptions of nuclear decay and half-lives, and can probe the significance of different coupled states over time.

In this thesis I will describe the theory, methods and results of a time-dependent coupled channels implementation. In Chapter 2 I outline the key theory from physics and mathematics needed for implementing the method. In Chapter 3, I step through the application of these theoretical points to solving the time-dependent Schrödinger equation numerically, and introduce Quantum Toolbox, a C++ library written to simulate dynamic nuclear reactions using this approach. In Chapter 4, I describe the results of testing Quantum Toolbox for precision and accuracy, in the latter case against known results. Finally, in Chapter 5, I describe the application of time-dependent coupled channels to the dissipative processes before and during fusion, and discuss the results.

Quantum Toolbox was written with the intent to extend it in the future. The initial results are very promising, with positive matches from tests against analytic and static coupled channels values. Further testing is needed to prove that this approach will solve current issues with static coupled channels.

Background theory

Before addressing the specifics of a time-dependent approach to coupled channels calculations, some key background material needs to be covered. The information presented in this section is written to introduce the reader to nuclear reaction dynamics at non-relativistic energies. Given the context in nuclear physics, a discussion of quantum modelling follows. This gives an explanation for why the coupled channels approach used in this thesis is so popular in nuclear physics, and where issues with coupled channels arise. I finally introduce the idea of a time-dependent form of coupled channels, and the reasons why this may be useful.

2.1 An overview of heavy ion reactions

Studies of heavy ion reactions are concerned with the physics of interacting nuclei, with the lightest element generally being categorised as "heavy" being Lithium. Here we consider reactions between heavy nuclei at energies near the fusion barrier energy, where the balance between Coulomb and nuclear forces leads to relatively gentle collisions. The purpose of these studies is many-fold, with the general goal to improve our understanding of the interplay between the internal structure of heavy ions, their macroscopic interactions, and the underlying quantum mechanics of the reactions. This feeds into our understanding of the reactions occurring in stars, and continues to be exploited to synthesise new elements, used as recently as 2002 in the discovery of element 118, Oganesson [6].

Reactions between two nuclei are described as a two-body system consisting of an incident 'projectile' ion and a (generally stationary) 'target' nucleus. The results of such a reaction are heavily dependent on the kinetic energy of the two nuclei, as well as two fundamental forces: the strong force and the electrostatic force. The strong force is a short-range strongly attractive force that acts between nucleons, and results in an attractive force between nuclei when their nucleons interact. The electrostatic force is a long-range force
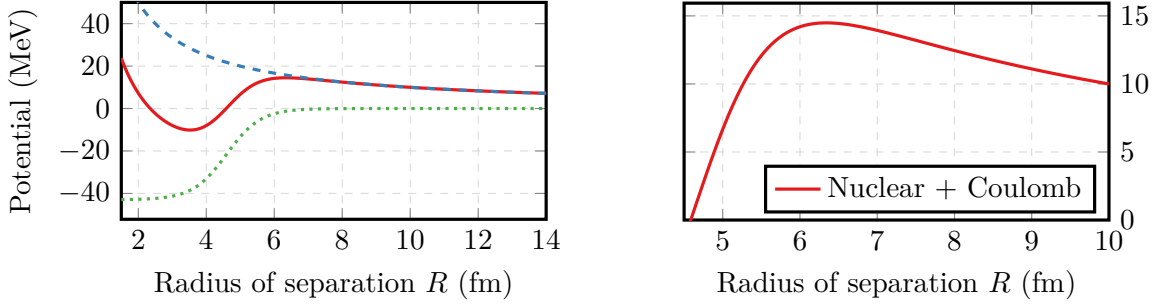
Figure 2.1: An example of the nuclear (dotted) and Coulomb (dashed) potential energies between two nuclei as a function of their separation R. The barrier (solid) appears near $R = 6$ fm, with the barrier height V_B shown on the right.

that acts between charged particles. It is described by Coulomb's law, and so is referred to as the Coulomb force [7]. In the case of interacting nuclei, each nucleus contains positively charged protons. The Coulomb force for nuclear reactions is therefore repulsive. The resulting effective nucleus-nucleus force is the sum of both Coulomb and nuclear parts, and depends on the inter-nuclear separation. At most separations the Coulomb force dominates, and at distances where there is some overlap between the nuclei the nuclear force takes over. There exists a tipping point at some intermediate separation. This exhibits itself as the 'barrier', a peak in the potential from the combined nuclear and Coulomb forces after which the nuclear potential begins to take over [8]. A diagram of the nuclear and Coulomb potentials, as well as their sum, is shown in Figure 2.1, with the barrier visible.

2.1.1   Types of nuclear reactions

The barrier allows nuclear reactions to be partitioned into two broad categories; *quasi-elastic reactions* and *capture reactions*. In the former the nuclei do not pass inside the barrier, either by tunnelling through it, or if the energy is high enough, passing over it. Any nuclear interactions are therefore weak. In the latter, the barrier is bypassed or overcome such that the nuclear interactions are strong. The component processes of these two categories will now be discussed.

Quasi-elastic reactions occur when the collision energy is not high enough to pass the barrier, and no tunnelling occurs. In this case the incoming nucleus scatters elastically or inelastically, and may see a transfer of a few nucleons. The signature of these is difficult to distinguish in the laboratory, hence why they are grouped together. Elastic collisions are very well understood, following the Rutherford scattering equations at energies well

COMPOUND NUCL.   QUASI-FISSION   DEEP INELASTIC
FISSION   SCATTERING
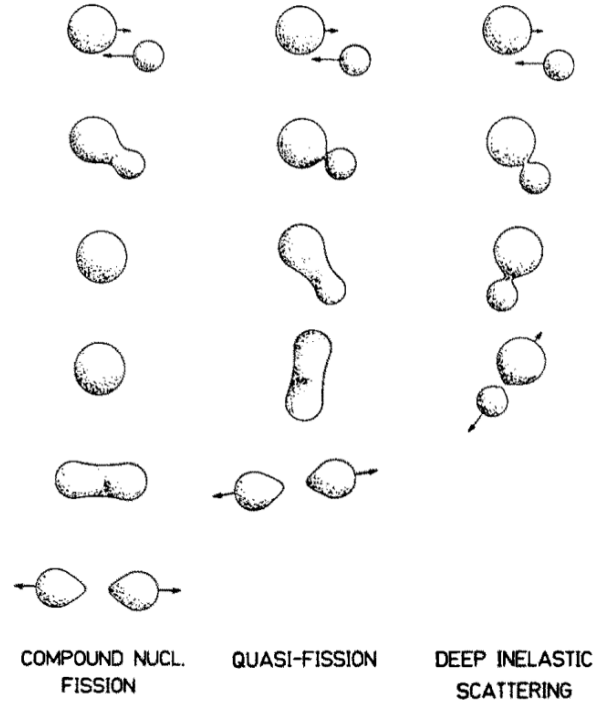
Figure 2.2: Schematic of the three types of capture reactions, depicting the differences in rotation and mass transfer. Figure originally published in [10].

below the barrier [9]. If some kinetic energy is transferred internally to one of the nuclei, exciting it, then inelastic scattering has occurred. The excited nucleus will later release this energy via nucleon or gamma emission, and since some kinetic energy has been lost the particles will slightly deviate from the Rutherford equations.

For the interacting nuclei to undergo a capture reaction the kinetic energy of the nuclei needs to be larger than the barrier to allow for barrier passing, or tunnelling needs to occur. As can be seen in Figure 2.1, in a capture reaction the barrier is overcome, and so nuclei can move close enough that the short-range nuclear force begins to contribute strongly along with the repulsive Coulomb force. Capture reactions can be subcategorised roughly by their contact time (the period over which the nuclei remain in contact). These sub-categories are known as *deep-inelastic scattering*, *quasi-fission* and *compound nucleus formation*, and are all strongly dissipative, converting kinetic energy into internal excitations.

Deep-inelastic scattering is a very rapid reaction, with some kinetic energy dissipated into internal excitation energy, but little transfer of mass between the nuclei. As sketched in Figure 2.2, the two nuclei become connected by a thin "neck". Exchange of nucleons through the neck can result in transfer of a large amount of kinetic energy into the nuclei,

but only a small net change in mass as few nucleons are transferred. The neck then breaks after a short period of time (approximately 1 zs, or 10^{-21} s), releasing the nuclei with lower kinetic energy [11]. The speed and lack of significant mass transfer lead some to contend that this is not actually a capture reaction, as this indicates that the nuclei may not have progressed to inside the barrier. It is because of this that deep-inelastic scattering is often said to be a reaction between quasi-elastic and capture reactions.

At the opposite extreme of capture reactions is compound nucleus formation, a much longer reaction. In compound nucleus formation the two interacting nuclei completely combine, forming a single nucleus with total mass and kinetic energy transfer. This compound nucleus is usually in a very excited state, and will decay, releasing or "evaporating" predominantly neutrons, but potentially protons and α-particles (helium nuclei) also. The products of this evaporation are known as "evaporation residues". For high angular momentum or mass, this compound nucleus is more likely to undergo fission, producing two approximately mass-symmetric nuclei, represented in Figure 2.2. This process is known as fusion-fission. The formation of the compound nucleus takes long enough that it will equilibrate, meaning that there is no dependence on any input variables other than angular momentum, parity and energy, as argued by Bohr [12]. Nuclear fusion generally refers to the formation of a compound nucleus.

Finally, in between these two capture reactions there exists quasi-fission, a moderately long, less well understood reaction, with some net mass transfer and complete kinetic energy dissipation [10]. As seen in Figure 2.2, the two nuclei become connected by a thicker neck than for deep-inelastic scattering, allowing more mass to flow between the two nuclei. This transfer is predominantly from the target nucleus to the projectile nucleus as equal sized nuclei minimises the potential energy of the system. The neck then breaks after some time.

For large nuclei the alternatives to compound nucleus formation occur more readily. Even after the barrier has been overcome, there is the chance for deep inelastic scattering or quasifission. It is for this reason that the "fusion" barrier, the combination of the nuclear and Coulomb potentials, is often referred to as the "capture" barrier for these heavier ions.

Capture reactions are highly dissipative, in both energy and mass, but the exact physics of this dissipation is not fully understood. An important reason for understanding the different component reactions in an experiment is to understand the fusion cross-section

of an experiment. The cross-section is a measure of characteristic area, some "space" in which nuclear reactions will occur. This is used in nuclear physics as an unnormalised measure of the probability that a reaction will occur, with a larger cross-sectional "area" more likely to be "hit" than a smaller one. For superheavy element formation reactions, where experiments can take many months or years of beam time, understanding fusion cross sections is critical. The cross section for evaporation residue formation σ_{ER} can be decomposed into a sum over angular momenta l as [13]

$$\sigma_{ER} = \frac{\pi \hbar^2}{2 \mu E} \sum_{l=0}^{\infty} (2l + 1) \, P_T \left(E, l \right) P_{CN} \left(E, l \right) P_{sur} \left(E, l \right) \tag{2.1}$$

where E is the kinetic energy, P_T is the probability for the nuclei to reach a separation close enough to touch, P_{CN} the probability that from this state a compound nucleus will form, and P_{sur} the probability that the compound nucleus will not fission. Unlike the other components, the probability P_{CN} that a compound nucleus will form is not well understood at all. There doesn't exist a theoretical model of nuclear reactions complete enough to describe P_{CN}, which involves the highly dissipative processes of deep inelastic scattering and quasifission. As a result measurement of compound nucleus formation is done experimentally, where it is difficult to distinguish between quasi-fission and fusion-fission, which is the largest component of compound nucleus formation events. The Oganesson experiment, where only 1 in 10^{19} projectile nuclei were detected as forming a compound nucleus of the new element, demonstrates that understanding P_{CN}, and the ability to detect fusion-fission events as well as evaporation residues, is very important for nuclear physics, as it would reduce the difficulty of compound nucleus detection [6].

To understand quasifission, it appears that further understanding of preceding reactions is needed. In recent studies, characteristics of quasifission have shown a strong isotopic dependence. In other words, a difference purely in the number of neutrons in the projectile has shown to be significant to quasifission outcomes [14, 15]. The difference in quasifission results implies that differences early in the collision are important in determining any subsequent evolution, as once the nuclei are considerably overlapping, the presence (or absence) of one or two nucleons in such a large system should be immaterial.

The relatively recent focus on such reactions, and in particular the less well understood deep inelastic scattering and quasifission, has identified a need for an updated theory. Theories in general provide a testing ground for effects less visible in experiments, and can also aide in experimental design. Later I will come to why there is a need for an updated

theory, but I will first outline the options available for modelling nuclear dynamics.

2.2 Models of nuclear interactions

Since the liquid drop model of the 1920s, a zoo of different models have been developed describe nuclear structure and reactions. They have had varying results, but none have been complete enough to address all the physics observed in nuclei [16]. This is often because the strong force cannot be measured directly, and deriving its effect on nuclei in scattering and fusion experiments has proven impossible so far. In this section I briefly cover the theoretical source of the strong force and why it is not overly useful in the context of this thesis. I then describe the key alternative models which are used in the field, focusing on two questions:

- Does the model include the physics needed?

- Is it possible to solve the model?

2.2.1 Quantum chromodynamics

Modelling of nuclei is particularly difficult due to their structure and the fundamental interactions involved. In reality, nuclei are composed of protons and neutrons, with these in turn made up of quarks. The interactions between these quarks are mediated by gluons and described by quantum chromodynamics (QCD) - the fundamental theory of the strong force. A full quantum model of two interacting nuclei is therefore a combination of the strong force between all the subatomic quarks, and the Coulomb force between the protons. With three quarks in each nucleon, even smaller systems will have hundreds of interaction terms in their Hamiltonian, with the size of the underlying Hilbert space scaling exponentially with the number of nucleons [17]. This is far too high-dimensional to solve, even for a supercomputer, and so alternative approaches must be considered. However, the number of these particles is too low for statistical techniques to be useful as they are in fluid and plasma physics. In fact, to sufficiently describe the physics of nuclei and their interactions some information about the system must be approximated away so the interactions can be reduced significantly.

2.2.2   The mean field and Hartree-Fock

The canonical next step is to consider only the mean field approximation of this complete many-body description. This involves a many-body Hartree-Fock Hamiltonian, which accounts for all two-particle interactions within and between the two nuclei. However, mean field theories such as this describe the physics of the "mean" field, for nuclear interactions resulting in a single trajectory in the most likely state. This treatment loses information about the wavefunction state, and thus prevents many-body tunnelling [18, 19]. Another problem with both of these cases is that, while they may be self-consistent as averaged potentials for each nucleon, they are only phenomenological. This is due to the lack of understanding of colour confinement and asymptotic freedom seen for low energy quarks, meaning the resulting nucleon-nucleon interaction is not known analytically [20–22]. Phenomenological interactions are therefore used which tend to be versions of the Skyrme potential [23].

2.2.3   Path integrals

The one common alternative is to use Feynman path integrals [24–26]. In this approach, one can find the propagator for a system, and integrate over all possible paths between the initial and final radial position and internal states. In some cases, the system is highly symmetric, and so the number of paths to integrate over can be reduced dramatically. In many cases the Wentzel-Kramers-Brillouin (WKB), or stationary phase approximation, is useful, giving the dominant behaviour of a system and simplifying the problem even further [27]. However, in the case of larger heavy ions, the complexity is too high, as the non-stationary terms will contribute significantly, and the symmetries do not reduce the number of computations enough. In addition, while the calculated values may be accurate using a path integral approach, it is much less easily interpreted and visualised than a direct coupled channels approach. While this lack of interpretability renders the path integral approach less generally useful than traditional coupled channels approaches, it is useful to keep in mind for complex systems. Approximations which are derived from the path integral approach, such as the no-Coriolis approximation, can greatly reduce the number of less influential channels, and thus the complexity of a coupled channels computation [28].

2.2.4   Coupled channels models

The minimum requirement for a model of fusion is the inclusion of tunnelling effects. Since the previously mentioned models are already phenomenological to some degree, a simpler phenomenological approach may be appropriate. Instead of describing the system completely from its fundamental interactions, or by phenomenological nucleon-nucleon interactions, bulk ion-ion potentials can be used to approximate the macroscopic physics of the interactions. Coupled channels approaches are one set of models which use this approach.

In coupled channels approaches the Hamiltonian approximates the mean effect of the strong force, usually in the form of a Woods-Saxon potential, and couplings between states approximate the major degrees of freedom of the complete system as single-particle wavefunctions [29]. This description in terms of wavefunctions includes tunnelling in each state, but the limited number of states renders the problem tractable to solve numerically while still including the dominant effects of nuclear structure.

There are several reasons why coupled channels are the preferred model for studying reactions such as deep-inelastic scattering and quasifission:

- Retains full wave description of the particles, and therefore tunnelling.

- Allows for explicit selection and study of internal states, and their impact on tunnelling.

- Most systems of equations are numerically solvable in a reasonable time period.

2.3   The formalism of coupled channels

The form of the nuclear Schrödinger equation used in the coupled channels equations is quite intuitive to understand, but deriving it provides one confidence in its authenticity, and further informs the nuclear physics context. In this section I present the most generally used mathematical formalism for accelerator experiments, generally following the presentation of Ian Thompson in Nuclear Reactions for Astrophysics [8]. I then show how the coupled channels equations arise from this formalism by including nuclear structure in the description.

In the frame of reference of an observer in the lab, accelerator experiments usually consist of an accelerated "projectile" A with mass m_A and velocity $\mathbf{u}_A$, and a stationary

Table 2.1: Differences between the laboratory and centre-of-mass frames of reference for a stationary target B.

	Velocity of A	Velocity of B	Total kinetic energy
Laboratory Frame	$\mathbf{u}_A$	$\mathbf{u}_B$	$\frac{1}{2}m_A\mathbf{u}_A^2 + \frac{1}{2}m_B\mathbf{u}_B^2$
Centre-of-mass Frame	$\mathbf{v}_A$	$\mathbf{v}_B$	$\frac{1}{2}\mu\mathbf{v}_{AB}^2$

"target" B with mass m_B and velocity $\mathbf{u}_B = 0$. Nuclear reactions occur very quickly, so we can assume that there are no externally acting forces. This allows a change of reference frame to one in which both particles are converging to a central point, which can freely be set to the origin [8]. This is known as the centre-of-mass frame. There is now only one kinetic energy term necessary, a function of the change in the separation of the particles A and B. The differences between the two frames are shown in Table 2.1, in which the reduced mass μ is defined as

$$\mu = \frac{m_A m_B}{m_A + m_B} \tag{2.2}$$

This change of frame can also be applied to the wavefunctions and potentials which make up the Schrödinger equation for two moving particles. For these two particles, there is a kinetic term for each, as well as a potential which acts between the two, dependent on the separation of their positions $\mathbf{r}_A$ and $\mathbf{r}_B$:

$$\left(-\frac{\hbar^2}{2m_A}\hat{\boldsymbol{\nabla}}_{\mathbf{r}_A}^2 - \frac{\hbar^2}{2m_B}\hat{\boldsymbol{\nabla}}_{\mathbf{r}_B}^2 + \hat{V}\left(|\mathbf{r}_A - \mathbf{r}_B|\right)\right)\Psi\left(\mathbf{r}_A, \mathbf{r}_B\right) = E\Psi\left(\mathbf{r}_A, \mathbf{r}_B\right) \tag{2.3}$$

In the centre-of-mass frame, the equivalent Schrödinger equation is reduced to a single kinetic term, and a potential term dependent on the relative separation of the particles $\mathbf{r}$

$$\left(-\frac{\hbar^2}{2\mu}\hat{\boldsymbol{\nabla}}_{\mathbf{r}}^2 + \hat{V}\left(r\right)\right)\Psi(\mathbf{r}) = E\Psi\left(\mathbf{r}\right) \tag{2.4}$$

where $r = |\mathbf{r}| = |\mathbf{r}_A - \mathbf{r}_B|$. This is very useful, as it has simplified the potential to one fixed around the origin. It also makes the representation of such a two-body collision more tractable, instead reframing it as a representative single particle with mass μ scattering with the origin.

To turn this from a standard Schrödinger equation to a set of coupled channels equations, a few more steps must be taken. First, one can note that Equation 2.4 represents energetic particles without any additional structure. This structure can be represented by a Hamiltonian H_0, which has an eigenbasis consisting of various eigenstates and associated

energies, parametrised by a generalised coordinate ζ [1]

$$\hat{\boldsymbol{H}}_0(\zeta)\phi_j(\zeta) = \epsilon_j\phi_j(\zeta) \tag{2.5}$$

Since the forces which create the potential V are dependent on the structure of the particles, it makes sense to allow it to also depend on ζ. Including this new Hamiltonian and modified interaction potential with the kinetic energy term in Eq. 2.4, a new total Hamiltonian can be written as

$$\hat{\boldsymbol{H}}_{tot}\left(\mathbf{r},\zeta\right) = \hat{\boldsymbol{H}}_0(\zeta) + \hat{\boldsymbol{V}}(r,\zeta) - \frac{\hbar^2}{2\mu}\hat{\boldsymbol{\nabla}}_{\mathbf{r}}^2 \tag{2.6}$$

which results in the Schrödinger equation

$$\left(-\frac{\hbar^2}{2\mu}\hat{\boldsymbol{\nabla}}_{\mathbf{r}}^2 + \hat{\boldsymbol{V}}\left(r,\zeta\right) + \hat{\boldsymbol{H}}_0(\zeta)\right)\Psi(\mathbf{r},\zeta) = E\Psi\left(\mathbf{r},\zeta\right) \tag{2.7}$$

The wavefunction $\Psi(\mathbf{r},\zeta)$, as an element of some Hilbert space, will have an expansion in terms of orthogonal eigenstates, which are independent and so separable into position eigenstates $\psi(\mathbf{r})$ and structural eigenstates $\phi(\zeta)$ as

$$\Psi(\mathbf{r},\zeta) = \sum_k \psi_k(\mathbf{r})\phi_k(\zeta) \tag{2.8}$$

Multiplying the Schrödinger equation 2.7 by an arbitrary structural eigenstate $\phi_j(\zeta)$ and integrating over ζ eliminates the $\phi_k(\zeta)$ terms, giving the set of equations

$$\left(-\frac{\hbar^2}{2\mu}\hat{\boldsymbol{\nabla}}_{\mathbf{r}}^2 + \epsilon_j\right)\psi_j(\mathbf{r}) + \sum_k V_{kj}\left(r\right)\psi_k(\mathbf{r}) = E\psi_j\left(\mathbf{r}\right) \tag{2.9}$$

one for each j, where

$$V_{kj}\left(r\right) = \int \phi_j(\zeta)^\dagger\hat{\boldsymbol{V}}(\mathbf{r},\zeta)\phi_k(\zeta)\,\mathrm{d}\zeta \tag{2.10}$$

are the potential matrix elements in the structural eigenstate basis. From now on I will refer to these eigenstates as just the "states" of a systems. These are the combined Coulomb and nuclear potentials for $j = k$, and potentials coupling the position eigenstates otherwise. The coupling potential magnitude V_{jk} describes the tendency of the system to transition from state k to state j. Finally, the system of equations in 2.9 can be rearranged

---

[1]Note: I am being purposefully general in this explanation, as understanding the form and purpose of the couplings is bogged down by the finer details.

to obtain the coupled channels equations, a set of coupled Schrödinger equations

$$\left(-\frac{\hbar^2}{2\mu}\nabla_{\mathbf{r}}^2 + V_{jj}\left(r\right) + \epsilon_n - E \right)\psi_n(\mathbf{r}) = -\sum_{k\neq j} V_{kj}\left(r\right)\psi_k(\mathbf{r}) \qquad (2.11)$$

Assuming a form for the potential matrix, including the potential and diagonal terms, and giving boundary conditions, these equations can be solved by iteratively applying the Numerov method. The boundary conditions are chosen to resolve the specific case in question, often the transmission amplitude or scattering matrix elements. As this technique is not applied in the time-dependent case, a discussion and derivation has been provided in Appendix A for the interested reader.

The formalism of channel coupling is frequently used throughout nuclear and atomic physics to describe the effects of internal states on a system of two interacting particles, and has been for over 30 years [3]. Particles are described quantum mechanically as in a coherent superposition of the internal states. The approach is a general one, only requiring the states and their coupling strengths are known.

Coupled channels methods are important precisely because they include a plurality of channels. Angular momentum states are the most common of these, as well as parity and isospin, which make up the nuclear structural energy states. The low lying of these structural states are discrete, and account for most of the impact channel couplings have in the majority of cases [30].

States in which nucleons have been transferred between the ions, or lost, can also be represented as channels. In inelastic reactions and capture reactions, there is some chance that the system will transition between states, and the coupled channels equations account for this possibility. Most of the information about these states can be found a priori from nuclear structure theory and experiment. However, the strength of coupling between these states cannot, and needs to be deduced from experiment or calculated from other models for each case.

2.4   Successes and failures of static coupled channels

In their seminal paper introducing coupled channels to nuclear fusion, Dasso *et al.* [3] initially used the equations to find the transmission rate of a two-state wavefunction incident on a simple square potential, an approximation for nuclear fusion with a fusion barrier. They also found the transmission for some systems more closely matching real
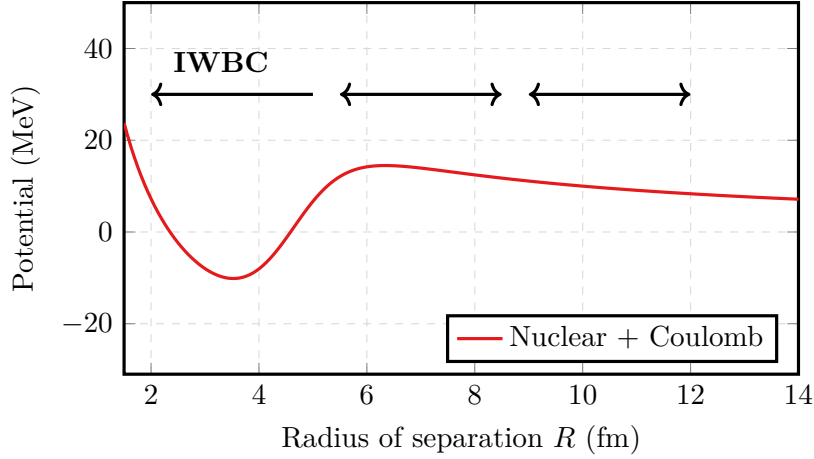
Figure 2.3: The fusion barrier, with a representation of the incoming wave boundary condition (IWBC) with only incoming flux permitted at radial separation inside the barrier.

nuclear interaction [3]. It was shown that channel coupling enhances transmission at energies below the Coulomb barrier. At these energies, this transmission is exactly quantum tunnelling. The enhancement can be easily seen in the degenerate energy constant coupling approximation, in which the coupled equations can be decoupled to illustrate that the barrier is split into two barriers; $V_B + V_C$ and $V_B - V_C$, where V_B is the barrier height and V_C is the strength of the coupling. This paper also found early evidence that even for very similar systems, slight differences in couplings and their strengths could lead to dramatically different amounts of transmission, and therefore fusion. However, this was far from a complete investigation, with only a few configurations of potential and couplings considered.

One issue with continuing to generalise the techniques introduced by Dasso *et al.* is that current coupled channels is not strictly a model for fusion. It is a model for scattering, where fusion is associated with channels outside the model space, but where there is no explicit description of the processes leading to the formation of a compound nucleus. This requires the imposition of non-physical boundary conditions to replicate experimental results by removing any possibility for the wavefunction to return from inside the barrier [31]. There are two forms of non-physical boundaries used. The most common is the incoming wave boundary condition, limiting momenta inside the fusion barrier to those propagating towards the nuclear centre-of-mass [32] as in Figure 2.3 (IWBC). This implies strong absorption at the centre-of-mass, simulating the channelling of the wavefunction into compound nucleus states.

More recently, in 2004 Newton *et al.* conducted a systematic study of above-barrier

capture cross sections into the use of the Woods-Saxon form of the nuclear strong force potential, and its use in coupled-channels simulations [5]. In these simulations the Woods-Saxon form of the nuclear potential was combined with the Coulomb potential to form the fusion barrier. Experimental results depart significantly from those predicted by coupled-channels simulations using this fusion barrier for heavy systems. A number of key factors contributed to this discrepancy, including a lack of accounting for fusion inhibition at low energies, no inclusion of inelastic processes such as nucleon transfer at high energies, and unaccounted dissipative effects in both cases. The dissipative effects studied show up most clearly in heavy systems due to their size, as dissipation appears to be stronger at larger distances from the radial centre $r = 0$. All of these factors together indicate one clear resolution; the use of dynamical calculations. This provides the direct motivation for this project. Dissipation is difficult or impossible to include in static coupled channels due to the solutions it finds. Therefore, a new time-dependent model is required to account for the strong dissipative effects seen experimentally.

2.5   Including time dependence in coupled channels

On top of the limited number of channels they include, many of the issues with coupled channels solutions stem from their nature as time-independent, only returning stationary states and their associated information. Most importantly, the static nature of coupled channels doesn't allow for dissipation. In open quantum systems, such as those studied in quantum optics, dissipation is usually included through some coupling to the environment, which allows for decoherence of the system. However, nuclear reactions are too fast and nuclei too heavy for any small environmental coupling to be influential. Without this environmental coupling, any time-independent approach using the Schrödinger equation is conservative, and so cannot remove flux from the coherently coupled channels with some non-physical potential or boundary condition. The alternative to this is to instead solve a time-dependent Hamiltonian system, which can include dissipation as a time-dependent temporary behaviour [33–35].

To include time dependence in coupled channels is as easy as solving the time-dependent instead of the time-independent Schrödinger equation, to find any intermediate state of the system. Time-dependent coupled channels can better describes the fused state of the nuclei as the capture of the wavefunction inside the region of the nuclear potential. This itself can be described by the nuclear potential coupling states. This will remove the

need for non-physical boundary conditions such as the imaginary potential. An additional benefit of this is that nuclear decay can be seen, as the wavefunction slowly leaks out of this nuclear region. This could give a quantum mechanical description and visualisation of fusion itself. It may also describe the time-dependence of capture processes such as quasifission. It is for these reasons that dynamic coupled-channels approaches should be investigated.

Time-dependent coupled channels approaches have been used outside of nuclear physics since as early as 2001, in theoretical atomic physics studies of positron-hydrogen collisions [36]. It has much more recently started seeing use in nuclear physics, as the needs for time dependence have become more clear. Tokieda and Hagino discussed a potential inclusion of energy dissipation as quantum "friction" in 2017, for which they used a time-dependent approach [37]. However, since this "frictional" dissipation occurs inside the nucleus, it is extremely difficult to verify such an approach, and the interpretation of their "friction" terms while tunnelling is unclear. In September of this year, a paper from the University of Surrey detailed the successful application of a time-dependent coupled channels method to replicate static coupled channels results for reactions of ^{16}O on ^{154}Sm [38]. This initial work is promising, but there is clearly much more that can be done to understand the method and its results, and to explore the advantages that time-dependent techniques bring to inherently time-dependent nuclear collisions.

The goal of this thesis is to contribute to this exploration, specifically as time-dependence relates to dissipative effects before and during fusion. In the next chapter I describe methods of solving the time-dependent coupled channels equations towards this purpose.

Solving time-dependent coupled channels equations

As discussed in the previous chapter, the coupled channels equations are simply second order systems of differential equations, and as such there exist many ways of solving them. In the vast majority of cases they is no known way to solve the system of equations exactly. Therefore, to have a code that is generally applicable to physical systems solutions must be found numerically. Any numerical approach will usually involve a balance between accuracy and computational complexity, and will ideally exploit properties of the Hamiltonian to optimise these aspects. In this chapter I cover the form of the time-dependent coupled channels equations, and methods to evolve a system numerically. The explanation is in general based on that in [36], but has been altered for clarity and to better match the nuclear context. I also cover points in the method where alternative approaches exist, and evaluate the benefits and downsides of these alternatives. I finally cover the general structure of Quantum Toolbox, a C++ library developed over the course of my project to implement time-dependent coupled channels simulations.

3.1 Time-dependent coupled channels formalism

Given the time-dependent Schrödinger equation for a system of wavefunctions

$$i\frac{\partial}{\partial t}\boldsymbol{\psi}(r,t) = \hat{\boldsymbol{H}}\boldsymbol{\psi}(r,t) \tag{3.1}$$

the potential, and thus the Hamiltonian, will have off-diagonal elements. Thus for an element of $\boldsymbol{\psi}$ the Schrödinger equation will be

$$i\frac{\partial}{\partial t}\psi_j(r,t) = \sum_k H_{jk}\psi_k(r,t) \tag{3.2}$$

which has solutions in terms of the time-evolution operator

$$\psi_j(r, t) = \sum_k S_{jk}(t - t_0)\psi_k(r, t_0) \tag{3.3}$$

where the time evolution operator $\hat{\boldsymbol{S}}$ has components

$$S_{jk}(t - t_0) = e^{-i(t-t_0)H_{jk}/\hbar} . \tag{3.4}$$

The operation of the time evolution operator can be discretised by introducing a small time interval Δt. A wavefunction after n timesteps will be denoted

$$\psi_j^{(n)}(r) = \psi_j(r, n\Delta t) . \tag{3.5}$$

In general, the Hamiltonian for a physical system is composed of a diagonal non-local operator $\hat{\boldsymbol{T}}$, representing the kinetic energy, a non-diagonal local operator $\hat{\boldsymbol{V}}$ which includes the potential and couplings between channels, and an internal Hamiltonian $\hat{\boldsymbol{H}}_0$ representing the internal states of the nuclei. Given this, the Hamiltonian can be written as

$$\hat{\boldsymbol{H}} = \hat{\boldsymbol{T}} + \hat{\boldsymbol{V}} + \hat{\boldsymbol{H}}_0 , \tag{3.6}$$

and so the time evolution operator becomes

$$\hat{\boldsymbol{S}}(\Delta t) = e^{-i\Delta t(\hat{\boldsymbol{T}} + \hat{\boldsymbol{V}} + \hat{\boldsymbol{H}}_0)/\hbar} . \tag{3.7}$$

3.2 Numerical methods for the time evolution operator

Given this form of the time evolution operator, a method of applying the exponential must be identified. Once a basis is chosen, the operators become matrices, but there is no clear way to apply the exponential of a matrix unless the matrix itself is diagonal. Separating the operators and then casting them to a basis in which they are diagonal is therefore the simplest approach. This requires that a default basis is chosen for the wavefunctions $\psi_j(r, n\Delta t)$.

3.2.1   Choosing a working basis

To simplify the visualisation of the evolving nuclei, and because most static coupled channels codes employ this method, a position basis as a spacial grid was chosen to represent the wavefunctions $\psi_j(r, n\Delta t)$. A discrete spacial basis is known to be accurate if it is detailed enough [39]. Many other representations of the wavefunctions can be used instead. Common choices are representations in terms of fixed functions, including Gaussian and Coulomb wavefunctions [40, 41]. This introduces more coding difficulty than the spacial grid, but can potentially improve computation efficiency if needed.

3.2.2   Separating the operators

In general the $\hat{\boldsymbol{T}}$, $\hat{\boldsymbol{V}}$ and $\hat{\boldsymbol{H}}_0$ operators don't commute, and so

$$e^{-i\Delta t(\hat{\boldsymbol{T}}+\hat{\boldsymbol{V}}+\hat{\boldsymbol{H}}_0)/\hbar} \neq e^{-i\Delta t\hat{\boldsymbol{T}}/\hbar}e^{-i\Delta t(\hat{\boldsymbol{V}}+\hat{\boldsymbol{H}}_0)/\hbar}. \tag{3.8}$$

Derived from the Baker-Campbell-Hausdorff (B-C-H) formula, a symmetrised Trotter product can be used to split the exponential terms into two half steps of $\hat{\boldsymbol{V}} + \hat{\boldsymbol{H}}_0$ and a whole step of $\hat{\boldsymbol{T}}$, accurate to second order in Δt [42]. Applying the symmetrised Trotter product formula here we have

$$\hat{\boldsymbol{S}}(\Delta t) = e^{-i\Delta t(\hat{\boldsymbol{V}}+\hat{\boldsymbol{H}}_0)/2\hbar}e^{-i\Delta t\hat{\boldsymbol{T}}/\hbar}e^{-i\Delta t(\hat{\boldsymbol{V}}+\hat{\boldsymbol{H}}_0)/2\hbar} + \mathcal{O}\left(\Delta t^3\right). \tag{3.9}$$

The Trotter product can be applied again, this time to the $\hat{\boldsymbol{V}} + \hat{\boldsymbol{H}}_0$ terms, to fully separate the operators as

$$\hat{\boldsymbol{S}}(\Delta t) = e^{-i\Delta t\hat{H}_0/4\hbar}e^{-i\Delta t\hat{V}/2\hbar}e^{-i\Delta t\hat{H}_0/4\hbar}e^{-i\Delta t\hat{T}/\hbar}e^{-i\Delta t\hat{H}_0/4\hbar}e^{-i\Delta t\hat{V}/2\hbar}e^{-i\Delta t\hat{H}_0/4\hbar} + \mathcal{O}\left(\Delta t^3\right) \tag{3.10}$$

with an overall error of $\mathcal{O}(\Delta t^3)$. This is a lower order Strang splitting, and can be rendered more accurate by splitting to higher order, at the cost of more computations [43, 44]. In fact, there are many elaborate splitting schemes which can be chosen from, all of which should improve the accuracy [45, 46]. Given wavefunctions at timestep n, their values can be approximated at the next timestep using this form of the time evolution operator

$$\psi^{(n+1)}(r) \approx e^{-i\Delta t\hat{H}_0/4\hbar}e^{-i\Delta t\hat{V}/2\hbar}e^{-i\Delta t\hat{H}_0/4\hbar}e^{-i\Delta t\hat{T}/\hbar}e^{-i\Delta t\hat{H}_0/4\hbar}e^{-i\Delta t\hat{V}/2\hbar}e^{-i\Delta t\hat{H}_0/4\hbar}\psi_k^{(n)}(r) \tag{3.11}$$

where each exponential term is applied in succession. Now that each term can be applied separately, a basis must be found for each in which the operator is diagonal, and so the exponential can be found.

3.2.3 Applying the potential energy operator

The local operator $\hat{\boldsymbol{V}}$ includes the potential and coupling terms. It is Hermitian, as all observables in quantum mechanics are, and as such it has a basis in which it is diagonal [47, 48]. So for some unitary transformation matrix $\hat{\boldsymbol{U}}$, $\hat{\boldsymbol{V}}$ can be decomposed as

$$\hat{\boldsymbol{V}} = \hat{\boldsymbol{U}}\hat{\boldsymbol{D}}\hat{\boldsymbol{U}}^{\dagger} \tag{3.12}$$

where $\hat{\boldsymbol{D}}$ is diagonal. This can easily be done efficiently for Hermitian matrices $\hat{\boldsymbol{V}}$ with a variety of algorithms, most commonly using a combination of the Lanczos and QR or divide-and-conquer algorithms [49–53]. Numerical packages are generally based on the LAPACK library, which includes these algorithms and more [54].

Using the diagonal representation of $\hat{\boldsymbol{V}}$ along with the definition of the exponential, the potential component of 3.11 can be simplified to a more usable form

$$\begin{aligned}
e^{-i\frac{\Delta t}{2\hbar}\hat{\boldsymbol{V}}} &= \sum_{k=0}^{\infty} \frac{\left(-i\frac{\Delta t}{2\hbar}\hat{\boldsymbol{V}}\right)^k}{k!} \\
&= \sum_{k=0}^{\infty} \frac{\left(-i\frac{\Delta t}{2\hbar}\hat{\boldsymbol{U}}\hat{\boldsymbol{D}}\hat{\boldsymbol{U}}^{\dagger}\right)^k}{k!} \\
&= \hat{\boldsymbol{I}} + \left(-i\frac{\Delta t}{2\hbar}\right)\hat{\boldsymbol{U}}\hat{\boldsymbol{D}}\hat{\boldsymbol{U}}^{\dagger} + \frac{1}{2}\left(-i\frac{\Delta t}{2\hbar}\right)^2\hat{\boldsymbol{U}}\hat{\boldsymbol{D}}\hat{\boldsymbol{U}}^{\dagger}\hat{\boldsymbol{U}}\hat{\boldsymbol{D}}\hat{\boldsymbol{U}}^{\dagger} + \dots \\
&= \hat{\boldsymbol{U}}\hat{\boldsymbol{U}}^{\dagger} + \hat{\boldsymbol{U}}\left(-i\frac{\Delta t}{2\hbar}\hat{\boldsymbol{D}}\right)\hat{\boldsymbol{U}}^{\dagger} + \frac{1}{2}\left(\hat{\boldsymbol{U}}\left(-i\frac{\Delta t}{2\hbar}\hat{\boldsymbol{D}}\right)^2\hat{\boldsymbol{U}}^{\dagger}\right) + \dots \\
&= \hat{\boldsymbol{U}}\left(\hat{\boldsymbol{I}} + \left(-i\frac{\Delta t}{2\hbar}\hat{\boldsymbol{D}}\right) + \frac{1}{2}\left(-i\frac{\Delta t}{2\hbar}\hat{\boldsymbol{D}}\right)^2 + \dots\right)\hat{\boldsymbol{U}}^{\dagger} \\
&= \hat{\boldsymbol{U}}e^{-i\frac{\Delta t}{2\hbar}\hat{\boldsymbol{D}}}\hat{\boldsymbol{U}}^{\dagger}
\end{aligned} \tag{3.13}$$

Since the exponential of a diagonal matrix is just the exponential of each diagonal element, the result in 3.13 can be directly applied to any wavefunction. This greatly simplifies the application of the potential term.

3.2.4   Applying the kinetic energy operator

Now that the $\hat{V}$ components of the time evolution operator have been manipulated to a usable form, the $\hat{T}$ component needs to be similarly simplified. The non-local operator $\hat{T}$, in its simplest form, is a function of the position Laplacian

$$\hat{T} = -\frac{\hat{\boldsymbol{\nabla}}_r^2}{2\mu} \tag{3.14}$$

The derivative $\hat{\boldsymbol{\nabla}}_r$ is equivalent to the conjugate, or wavenumber, operator $\hat{\boldsymbol{k}} = \hat{\boldsymbol{p}}/\hbar$ under Fourier transformation

$$\hat{\boldsymbol{\nabla}}_r \xrightleftharpoons[\mathcal{F}^{-1}]{\mathcal{F}} i\hbar\hat{\boldsymbol{k}} \tag{3.15}$$

which is local in conjugate/Fourier space. This is a scaled form of the momentum operator $\hat{\boldsymbol{p}} = \hbar\hat{\boldsymbol{k}}$. Transforming the wavefunction to conjugate space allows for application of the local wavenumber operator instead of the Laplacian.

$$\begin{aligned} e^{-i\Delta t\hat{\boldsymbol{T}}/\hbar} &= \exp\left(i\Delta t\frac{\hat{\boldsymbol{\nabla}}_r^2}{2\hbar\mu}\right) \\ &= \hat{\mathcal{F}}^{-1}\exp\left(-i\Delta t\frac{\hbar\hat{\boldsymbol{k}}^2}{2\mu}\right)\hat{\mathcal{F}} \end{aligned} \tag{3.16}$$

The fast Fourier transform is computationally cheap, with complexity at most $\mathcal{O}(n\log(n))$. This can be improved if the number of grid points has only small prime factors, as the most common split-radix FFT algorithm can speed up computations through factorisation of the grid [55]. Error in the FFT exists due to the Nyquist Sampling Theorem, which explains why high frequency, large k, parts of the wavefunction will be lost. However, this maximum k can be set high enough to not remove any important components of the wavefunction.

3.2.5   Alternatives methods for the kinetic operator

The application of the kinetic operator has the largest variety of alternatives, many not using Fourier transformation at all. In their recent paper the team at the University of Surrey expanded the kinetic operator in terms of Chebyshev polynomials and their derivatives. These can then be applied directly to the kinetic operator [38]. Another alterative is to approximate the kinetic operator for each position as an operation on the neighbouring points, through a finite difference approach. This has been used successfully for time-dependent coupled channels in atomic physics [36]. Further possible methods

include various other finite difference methods, as well as Crank-Nicolson, Chebyshev polynomial and Lanczos methods [56–58].

It is difficult ab initio to know which approach is ideal, given that they vary differently with increased detail, including to the splitting chosen earlier. However, as the key values for this project are the wavefunction densities in conjugate space, the use of the Fourier transform to also localise the kinetic operator allows for reuse of code.

3.2.6 Applying the structural Hamiltonian operator

Finally, the internal state Hamiltonian $\hat{\boldsymbol{H}}_0$ needs to be applied to the wavefunction. This step is the simplest, as the coupled channels equations are already represented in the state basis, in which $\hat{\boldsymbol{H}}_0$ is diagonal. The entries of $\hat{\boldsymbol{H}}_0$ are $H_{jj} = \epsilon_j$, where ϵ_j is the energy of the internal state relative to the ground state entrance channel.

3.3 Implementing time-dependent coupling simulation

To derive information about a nuclear system using a coupled channels approach, the equations need to be formed and then solved. These results indicate that a split step Fourier method is fast and accurate enough, applying the operators in full through diagonalisation, and importantly is reasonably simple to implement. It is for these reasons that a symmetric split step Fourier method will be followed after constructing the coupled channels equations. However, before this step, a functional form for the wavefunctions needs to be discussed, with which to do these computations.

3.3.1 Gaussian wavepackets

The method previous asserts that a solution can be found for a system of coupled time-dependent Schrödinger equations, given an initial condition. This effectively assumes that there exists a suitable initial condition to choose, one which closely approximates the system in question. In this case, the best choice is something that looks like a particle; localised in space and momentum. The ideal choice is a wavepacket, a wavefunction that is zero everywhere except a small local region. The most common of these is the Gaussian wavepacket, which has normally distributed magnitude around some central point. From this point on, "wavepacket" will refer explicitly to Gaussian wavepackets.
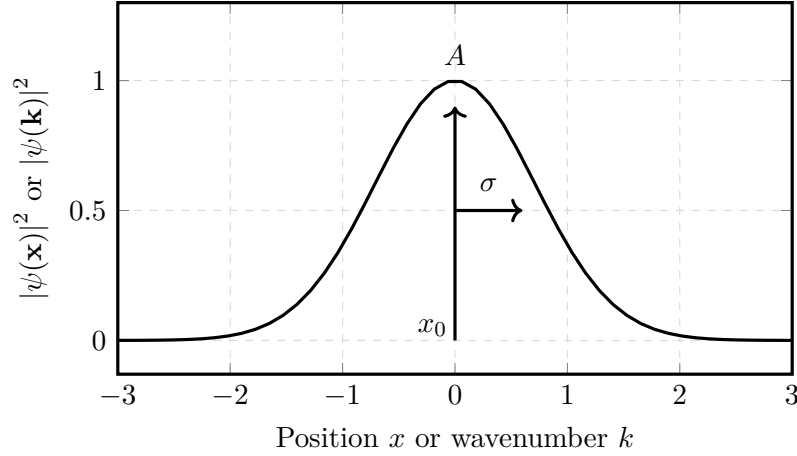
Figure 3.1: The general form of a Gaussian wavepacket, in either position space or conjugate space.

Stationary wavepackets have the form

$$\psi(x) = Ae^{-\frac{(x-x_0)^2}{2\sigma}} \tag{3.17}$$

where x_0 is the centre of the wavepacket, σ is the width and A is a constant. In our case A is chosen such that the wavepacket is normalised:

$$\int_{-\infty}^{\infty} |\psi(x)|^2 \; \mathrm{d}x \tag{3.18}$$

This stationary wavefunction can be "boosted" and given some mean energy E by including a phase

$$\psi(x) = Ae^{ikx - \frac{(x-x_0)^2}{2\sigma}} \tag{3.19}$$

where $k = \sqrt{2\mu\,(E - \epsilon)}/\hbar$ is the wavenumber corresponding to E for the channel with internal energy ϵ. The wavepacket has a "group velocity", the mean velocity of all components, with is dependent on this energy E.

$$\langle v \rangle = \frac{\langle p \rangle}{\mu} = \sqrt{\frac{2E}{\mu}} \tag{3.20}$$

This means that the "speed" of the wavepacket outside any potential, and thus its position, can be known a priori. Even after experiencing some interaction with a potential, knowing the rate of spreading and group velocity allows for calculation of an approximate position as a function of time, meaning simulations can be run knowing the correct t_f without detailed observation of the wavepacket evolution.

At $t = 0$, wavepackets have minimum uncertainty [59].

$$\Delta x \Delta p = \hbar/2 \qquad (3.21)$$

In other words, position and momentum are as localised as is quantum mechanically possible, which is to be expected of nuclei [60]. A wavepacket, as it has a Gaussian form, is also Gaussian in the conjugate space [59]. This means it contains components with energies distributed around its mean energy, meaning nuclear observables can be calculated as a function of energy purely from a single wavepacket simulation. This spread of energies requires that parts of the wavepacket move at different velocities, and thus spread over time. The spread of a wavepacket can be calculated as a function of time

$$\sigma^2(t) = \sigma_0^2 + \frac{t^2}{4m^2\sigma_0^2} \qquad (3.22)$$

For the purposes of this thesis, finding transmission probabilities and fusion rates, it is best if the wavepacket has significantly populated momenta, and thus energy states, widely around the mean energy. Since a wider spread in momenta means a narrower spread in position, by the Pauli exclusion principle, a minimal width in position space at the beginning of any simulation is ideal. This then allows matching of the various initial and final energy components of the wavefunction, so that nuclear observables can be calculated robustly for many energies. An issue with this, however, is that $\sigma^2(t) \propto t^2\sigma_0^{-2}$, and so spreads much faster for narrower initial wavepackets. This spreading needs to be accounted for in any implementation of the code, to prevent wavefunction interaction with the grid boundary.

3.3.2   Choosing the couplings

Now that a form of the wavefunction has been chosen, the couplings between these wavefunctions is the next component of the solution. The choice of channels is one of the key problems with coupled channels methods. As discussed previously, there are ways to constrain these channels through the use of mean field and path integral methods. Knowledge about the vibrational and rotational states of nuclei are known from nuclear structure theory, and can be used as well. However, a more significant issue is that of the couplings themselves. It is not known exactly what form the coupling potentials take, particularly for coupling deeper into the fusion barrier, in regions where deep inelastic and neutron

transfer processes take place. This work presented later in this thesis is focused on the form of these couplings and their general effects, not requiring physically exact channels and couplings. The interested reader can find detailed discussion of the most common couplings in the PhD of Kouichi Hagino, the creator of the static coupled channels code CCFULL [30].

3.3.3   The final propagator

Based on the techniques presented, diagonalisation was chosen for the potential operator, with the kinetic operator applied in conjugate space through use of the FFT and the internal Hamiltonian applied directly. Using these operations, it becomes relatively simple to apply the time evolution operator

$$
\hat{\boldsymbol{S}}(\Delta t) \approx e^{\left(-i\Delta t\hat{\boldsymbol{H}}_0/4\hbar\right)} e^{\left(-i\Delta t\hat{\boldsymbol{V}}/2\hbar\right)} e^{\left(-i\Delta t\hat{\boldsymbol{H}}_0/4\hbar\right)} e^{\left(-i\Delta t\hat{\boldsymbol{T}}/\hbar\right)} e^{\left(-i\Delta t\hat{\boldsymbol{H}}_0/4\hbar\right)} e^{\left(-i\Delta t\hat{\boldsymbol{V}}/2\hbar\right)} e^{\left(-i\Delta t\hat{\boldsymbol{H}}_0/4\hbar\right)}
$$

$$
= e^{\left(-i\Delta t\hat{\boldsymbol{H}}_0/4\hbar\right)} \hat{\boldsymbol{U}} e^{\left(-\frac{i\Delta t\hat{\boldsymbol{D}}}{2\hbar}\right)} \hat{\boldsymbol{U}}^\dagger e^{\left(-i\Delta t\hat{\boldsymbol{H}}_0/4\hbar\right)} \hat{\mathcal{F}}^{-1} e^{\left(-\frac{i\Delta t\hbar\hat{\boldsymbol{k}}^2}{2\mu}\right)} \hat{\mathcal{F}}
$$

$$
\cdot e^{\left(-i\Delta t\hat{\boldsymbol{H}}_0/4\hbar\right)} \hat{\boldsymbol{U}} e^{\left(-\frac{i\Delta t\hat{\boldsymbol{D}}}{2\hbar}\right)} \hat{\boldsymbol{U}}^\dagger e^{\left(-i\Delta t\hat{\boldsymbol{H}}_0/4\hbar\right)}
$$

$$
\tag{3.23}
$$

Implemented in code, this timestepping equation becomes Algorithm 1.

Algorithm 1 Time evolution of coupled channels

Initialise timestep Δt, initial time t_i and final time t_f
Initialise spacial and conjugate grids X and K
Initialise vector of reaction channels Ψ
Initialise split step terms V, T and H_0
$t \leftarrow t_i$
while $t < t_f$ **do**
    Diagonalise V
    Apply H_0 step to Ψ ▷ (1)
    Apply V step to Ψ ▷ (2)
    Apply (1) again
    FFT Ψ
    Apply T step
    Inverse FFT Ψ
    Apply (1), (2) and (1) again
    $t \leftarrow t + \Delta t$
end while

This algorithm is presented in a way which works for the Dirac (interaction) picture and the Schrödinger picture, as both the operators and the states can evolve with

time. Since these pictures are equivalent, it is computationally more efficient to assume the Schrödinger picture, allowing the static operators to be defined only once outside the timestepping **while** loop, meaning the diagonalisation routine only needs to be performed once. Numerically, this lack of time dependence means that the product $\exp\left(-i\Delta t\hat{\boldsymbol{H}}_0/4\hbar\right)\hat{\boldsymbol{U}}\exp\left(-\frac{i\Delta t\hat{\boldsymbol{D}}}{2\hbar}\right)\hat{\boldsymbol{U}}^\dagger\exp\left(-i\Delta t\hat{\boldsymbol{H}}_0/4\hbar\right)$ can be stored as a single matrix, which only needs to be applied to the wavefunction twice per timestep.

3.4 Overview of the code structure in the Quantum Toolbox library

In this final section I briefly discuss the main aspects of the code, Quantum Toolbox, used throughout the later chapters of this work. The link for the Quantum Toolbox GitHub repository can be found in Appendix B.

Quantum Toolbox is a codebase for time-dependent quantum simulations, with a focus on nuclear reactions. It is an object-based code written in C++ , with extensive use of the Eigen linear algebra library [**?**].

3.4.1 Eigen

Eigen is a popular library for linear algebra on C++ . In Quantum Toolbox it is particularly important for basic operations and Fourier transformation, as it stores data contiguously in memory, resulting in very fast vectorised operations. Eigen has a convenient syntax, which allows the code to be easily extended. It is additionally convenient because it is a header-only library, meaning that it doesn't require building or installing. Its headers are saved in the Quantum Toolbox repository, meaning it is freely downloadable and usable immediately.

All of the classes in Quantum Toolbox make use of Eigen, with five of them comprising the bulk of the code functionality.

3.4.2 Quantum Toolbox classes

The base class on which all other classes are defined in Quantum Toolbox is the Grid.

Inputs The number of grid steps $N-1$, the minimum and maximum points.

Function Stores arrays for the position x and momentum/wavenumber grids k.

The conjugate grid is known from the spacial grid, as

$$k_{\text{max}} = \frac{\pi}{\Delta x} \tag{3.24}$$

and similarly

$$\Delta k = \frac{2\pi}{x_{\text{max}} - x_{\text{min}}} \tag{3.25}$$

where Δx is the spacial grid step size, and Δk the step in the conjugate grid [59].

The next classes are the Wavefunction and Potential classes. Starting with the Potential class:

Inputs A Grid class object.

Function Stores an array for a specific potential V, with additional functions to initialise this potential with common forms such as the Woods-Saxon.

Clearly the Potential is very simple, and is only there to be able to create, manipulate and access the form of the potential. Moving on to the Wavefunction class:

Inputs A Grid class object, and optionally the reduced mass μ and the internal energy ϵ.

Function Stores arrays for the position wavefunction ψ and the corresponding conjugate wavefunction ψ_k. Updates ψ from ψ_k and ψ_k from ψ. Many additional functions exist for wavefunction initialisation and measurement in either grid.

Conversion between ψ and ψ_k is done by Fast Fourier Transformation, specifically the implementation used by Eigen is the Fastest Fourier Transform in the West.

The fourth class, the System, is the most significant.

Inputs A Wavefunction and a Potential object, with the possibility of adding more for coupled channels systems.

Function Propagates coupled channels systems. Stores wavefunctions, potentials and arrays to log their values. Additional functions include calculation of transmission and reflection rates.

The System implements the split-step Fourier time-evolution described earlier in this chapter. This works by simultaneously applying the $\hat{\boldsymbol{H}}_0$ and $\hat{\boldsymbol{V}}$ steps to the vector of spacial wavefunctions for all grid points. The wavefunctions are then Fourier transformed, the

kinetic operator $\hat{\boldsymbol{T}}$ is applied, and the inverse Fourier transform converts the wavefunctions back to the spacial grid. The $\hat{\boldsymbol{H}}_0$ and $\hat{\boldsymbol{V}}$ steps are then applied again.

The final class is the Plotter class.

Inputs A System object.

Function Visualise System propagation. Visualise wavefunctions.

The visualisation in the Plotter class is done with gnuplot. Data is piped to a gnuplot instance using the gnuplot-iostream library.

Calculation testing and benchmarks

Any code worth its salt should be proven against testing before use. Quantum Toolbox and its time-dependent coupled channels implementation is no exception to this rule. While the numerical approaches discussed in Chapter 3 give some indication that the approximation is accurate, implementations in code introduce their own errors. Conveniently, known results for coupling-free and single-coupling cases from static coupled-channels methods provide a good benchmark for testing the validity of this time-dependent approach, and any error that may come with it.

In this chapter I discuss the results of testing Quantum Toolbox. I start by quantifying the most basic forms of inaccuracies in the code, errors in storage and mathematical operations. I then verify the functionality without couplings on the analytic result for a square potential, and use this case to quantify the numerical error introduced by the timestep and position step sizes Δt and Δx. I finally confirm the functionality of the coupled channels on two two-channel cases, reproducing results previously found using static coupled channels codes. In all test cases but the last, the internal Hamiltonian is the zero matrix, and so has no influence on the solutions.

4.1 Contributors to numerical error

It is clearly important to know how much error accrues through the time evolution algorithm due to the previously discussed splitting approximations. However, there are other significant sources of error which first need to be understood to contextualise the algorithmic error. These include the numerical error in arithmetic operations to to the inexact storage of floating point numbers, and the error introduced through Fourier transformation on a limited grid.

4.1.1 Numerical error from floating point roundoff

One definition of error which may prove useful is that of machine epsilon ε, also known as the unit roundoff. Machine epsilon is specifically defined as the difference between 1 and the next representable number for a given floating point data type. What this means in practice is that if a value is computed using floating point arithmetic, it will generally be rounded above or below its real value, dependent on the data type precision. Half of this machine epsilon is a good estimate for the uncertainty in a value under floating point arithmetic. Double precision floating point numbers (i.e. doubles) have been used throughout Quantum Toolbox, and have a machine epsilon of approximately 2.22×10^{-16} [61], giving an uncertainty of approximately 10^{-16}.

(a) Initial wavepacket **(b)** Wavepacket after 1 step

(c) Wavepacket after $10^4 \, \mathrm{fm} \, c^{-1}$
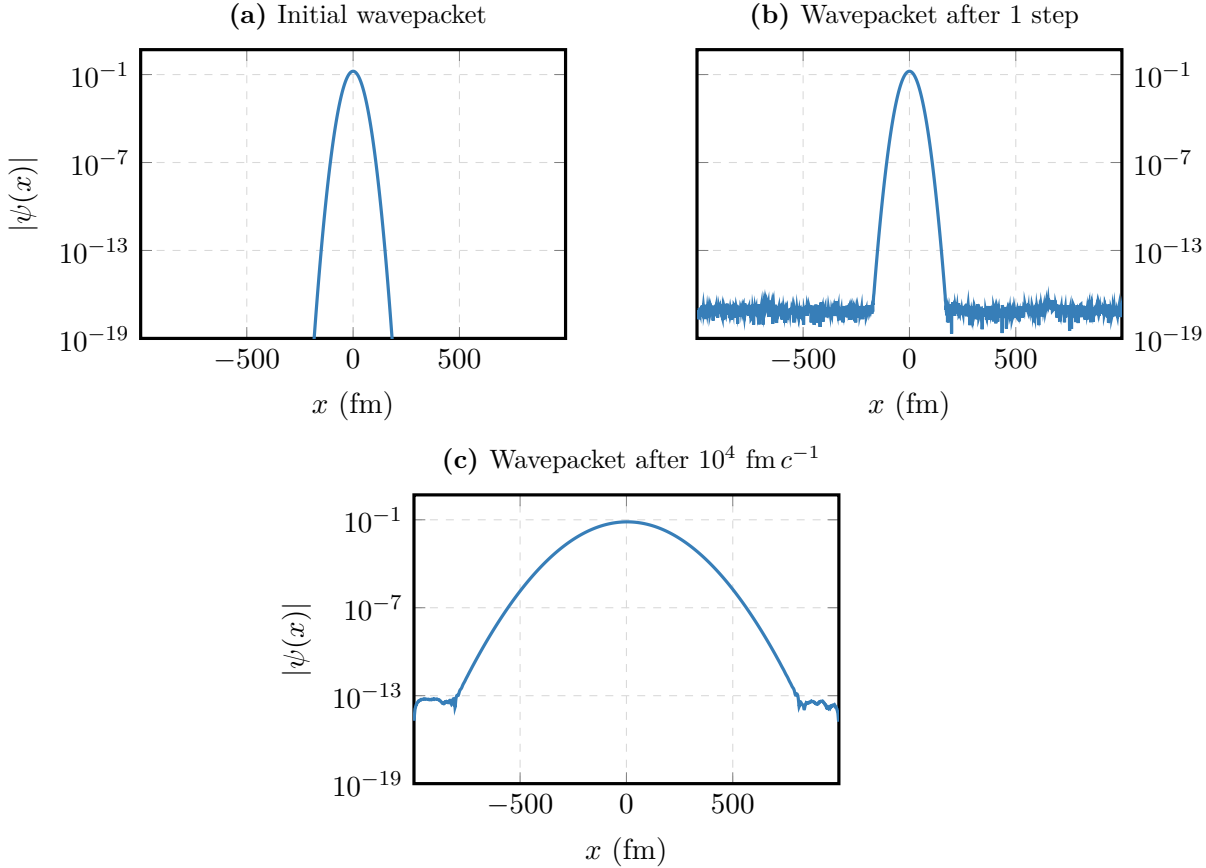
Figure 4.1: Log scale plots of a wavepacket magnitude over time. Variation in values close to zero indicate an intrinsic error of 10^{-16} in the floating point roundoff, which propagates up to 10^{-13} on the timescales of tunnelling.

This can be visualised in Quantum Toolbox by representing a Gaussian wavepacket on a grid under no potential. As doubles store small input values accurately down to below 10^{-300}, the Gaussian wavepacket in 4.1a is almost perfectly represented [62]. Some

floating point arithmetic is performed to evolve this wavepacket by one time evolution step, which results in some rounding error. The result in 4.1b shows that the smallest values agree with this definition, as they appear to have been rounded from approximately 0 to a magnitude of around 10^{-16}. The aggregation of this rounding error can be seen in 4.1c, which has been evolved up to $10^4\,\mathrm{fm}\,c^{-1}$, an order of magnitude more time than most nuclear interactions I will consider in this thesis. At this time, the wavepacket has become less localised due to the spread in momenta. At the same time, the size of the errors has increased to a magnitude of 10^{-13}. This gives some indication that the actual uncertainty dealt with in completed simulations will be larger than just the roundoff error.

The propagation of the wavefunction in this case has a zero potential term, and thus the error is only dependent on the error associated with the kinetic term. Application of the kinetic energy operator transforms to reciprocal space (k-space) and back using the Fast Fourier Transform, so it is useful to know the error introduced by this operation.

4.1.2   Numerical error from the Fast Fourier Transform

The Fast Fourier Transform (FFT) is an efficient implementation of the discrete Fourier transform. These transforms are not complete, having a resolution dependent on the endpoints and the number of grid points defined in the code. The uncertainty in the Fast Fourier Transform values depends on the implementation. For the Fastest Fourier Transform in the West (FFTW) [63] used in Quantum Toolbox, the underlying algorithm is a version of the Cooley-Tukey algorithm [64]. This has an uncertainty of $\mathcal{O}(\varepsilon_m\sqrt{\log N})$ where N is the number of grid points and ε_m is machine epsilon for the given data type. For doubles, and on grids of $N = 10^3$ to $N = 10^6$, this comes to an uncertainty of $\mathcal{O}(10^{-16})$. The Fastest Fourier Transform in the West authors provide benchmarks on various CPU platforms comparing the accuracy of FFTW to other FFT packages [65]. The relative error given in these benchmarks is similar over all platforms, with values around 1.10×10^{-16}.

To check this benchmarked relative error, a purely real Gaussian wavepacket in Quantum Toolbox was transformed into k-space using the FFT, and then inverted back to position space. The difference between the initial and final wavefunctions was computed, both for the real and imaginary components a and b in rectangular form $a + ib$, and their respective amplitudes and phases r and φ in polar form $re^{i\varphi}$. The mean and standard deviation of these differences is presented in Table 4.1.

Table 4.1: Differences between $\psi(x)$ and $\hat{\mathcal{F}}^{-1}\hat{\mathcal{F}}\psi(x)$ using FFTW. For each representation, rectangular and polar, the average and standard deviation of the differences in each coefficient are shown.

N	Rectangular $(a + ib)$		Polar $(r\exp(i\varphi))$	
	$\hat{a}$	$\hat{b}$	$\hat{r}$	$\hat{\varphi}$
10^3	$(-0.3 \pm 4.6) \times 10^{-17}$	$(0.03 \pm 1.2) \times 10^{-17}$	$(0.6 \pm 4.6) \times 10^{-17}$	0.09 ± 0.69
10^4	$(-0.6 \pm 2) \times 10^{-17}$	$(-0.01 \pm 1.7) \times 10^{-17}$	$(1.1 \pm 2.1) \times 10^{-17}$	0.005 ± 0.75
10^5	$(-0.05 \pm 1.4) \times 10^{-16}$	$(-0.1 \pm 7.6) \times 10^{-17}$	$(0.6 \pm 1.4) \times 10^{-16}$	0.003 ± 0.68
10^6	$(-0.06 \pm 3.3) \times 10^{-16}$	$(-0.03 \pm 7.9) \times 10^{-17}$	$(0.6 \pm 3.3) \times 10^{-16}$	0.001 ± 0.71

The errors shown in the table, that is the differences introduced by fast Fourier transformation, agree with the Cooley-Turkey uncertainty estimate. The coefficients on average match, and so the transformed values are near evenly distributed above and below the actual values. The standard deviation appears on the same order of magnitude as the floating point roundoff error. This does not improve with higher values of N, specifically because the k values for the original Gaussian wavepacket are already included for low N. The larger N just adds unpopulated high frequency k, which all introduce floating point error significant relative to their value. It is most important to note that while the magnitude of the difference is generally small, the complex phase is significantly different. This comes from the zero complex coefficient of the original values being changed through floating point roundoff, which is significant compared to the near-zero real values of the wavefunction outside the wavepacket. In the region where the wavepacket is defined, the original and transformed wavefunction are in essence identical, as the roundoff is insignificant compared to the actual value.

For both the evolving wavepacket and the FFT, the largest errors observed were on the order of 10^{-13}. In the next tests, Quantum Toolbox will be compared to analytic results for the uncoupled square barrier. The error estimates given here allow values to be separated into those that are noise-dominated, with values near $\mathcal{O}(10^{-13})$, and those that are not. For those that aren't dominated by noise, the algorithmic error should be visible, and thus a dependence of this error on Δt and Δx can be found.

(a) $t = 0 \ \mathrm{fm}\, c^{-1}$ **(b)** $t = 14 \ \mathrm{fm}\, c^{-1}$
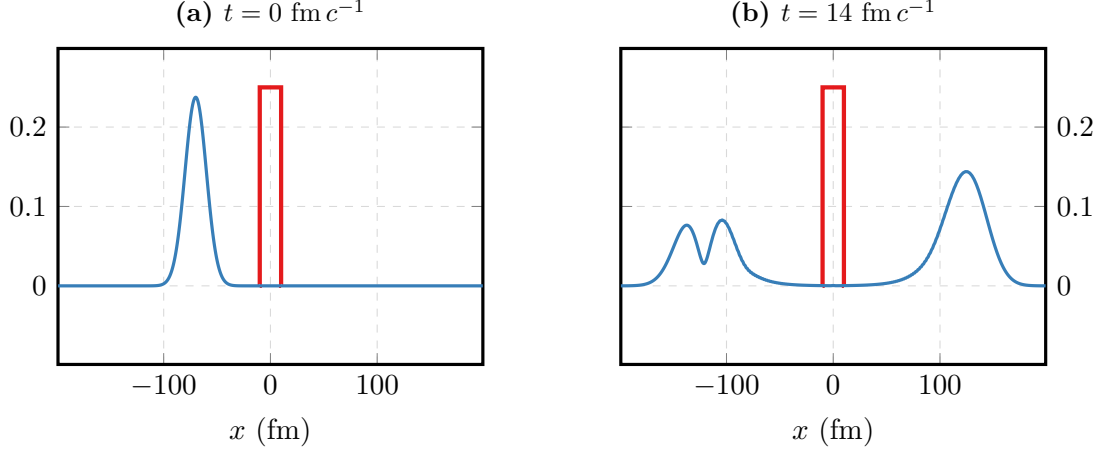
Figure 4.2: A wavepacket before (a) and after tunnelling (b) through a square barrier free of couplings.

4.2   Verification against analytic results for tunnelling

Having some confidence that the numerical error of the code is low enough for simulation purposes, and some estimates for error introduced through floating point roundoff and fast Fourier transformation, the next step is to test against analytic results. In the first test, a square barrier with no couplings was considered, to ensure that Quantum Toolbox applies the time-evolution operator correctly. This was first computed for very small Δx and Δt to remove as much computational error as possible, and check that the results match. Given the functionality of the code, this same case was then computed for a variety of Δx and Δt. Comparing results with analytic values, the error was found as a function of these two variables, giving uncertainty estimates for later calculations.

In both these cases the incident wavefunction was a Gaussian wavepacket, as it is localised and contains all energies near the barrier. The qualitative behaviour of this wavepacket is shown in Figure 4.2.

4.2.1   A single channel incident on a square barrier

In this test I considered a Gaussian wavepacket incident on a square barrier at various potentials. The barrier a width of 5 fm, enough to see the effects of tunnelling. The wavepacket was given an initial variance of 2.5 fm, to ensure a large enough spread of energies.

The transmission rates are a standard result known analytically, with three equations

giving the transmission below, at and above the barrier respectively

$$T(E < V_0) = \left(1 + \frac{V_0^2 \sinh^2(k_- a)}{4E(V_0 - E)}\right)^{-1} \tag{4.1}$$

$$T(E = V_0) = \left(1 + \frac{k_0^2 a^2}{4}\right)^{-1} \tag{4.2}$$

$$T(E < V_0) = \left(1 + \frac{V_0^2 \sin^2(k_+ a)}{4E(E - V_0)}\right)^{-1} \tag{4.3}$$

where $k_- = \frac{\sqrt{2(V_0 - E)}}{\hbar^2}$, $k_0 = \frac{\sqrt{2V_0}}{\hbar}$ and $k_+ = \frac{\sqrt{2(E - V_0)}}{\hbar^2}$ [8].

The initial wavepacket has a spread of positive wavenumbers k, as it is moving in the positive x direction, to the right. These wavenumbers are associated with a particular energy. After interaction with the barrier, the resulting wavefunction bifurcates into a left-moving reflected component and a right-moving transmitted component. The Fourier representation of the wavefunction also bifurcates, splitting into a positive and negative k component. This is because the right-moving transmitted component is composed of positive wavenumbers, and the left-moving reflected component negative wavenumbers. The whole system is conservative, so the total wavefunction density for each energy E corresponding to a positive wavenumber k and negative $-k$ must remain the same as the initial density [59]. The density of the right-moving transmitted components at each energy can be compared to their initial magnitude to get the transmission probability

$$T_{E(k)} = \frac{|\psi_f(k)|^2}{|\psi_i(k)|^2} \tag{4.4}$$

For example, if the original wavefunction has a probability density at k of 0.5, and a final density at this k of 0.25, then the transmission probability is 0.5, or 50%.

The transmission for several barrier heights was initially computed with small timesteps of $\Delta t = 10^{-2}$ fm c^{-1} and a detailed grid of $N = 16384$ points with endpoints ± 500 fm, resulting in a detailed grid with $\Delta x = 0.061$ fm to minimise numerical error.

In Figure 4.3 both the analytic and simulated transmissions are shown for several barrier heights at various energies. The results are extremely similar, with very low error for all but the barrier height of $V_0 = 10$ MeV. In this case, the energy is so low that the wavepacket energy spread is significant relative to its mean energy, meaning some lower energy components became trapped inside the square barrier while the higher energy
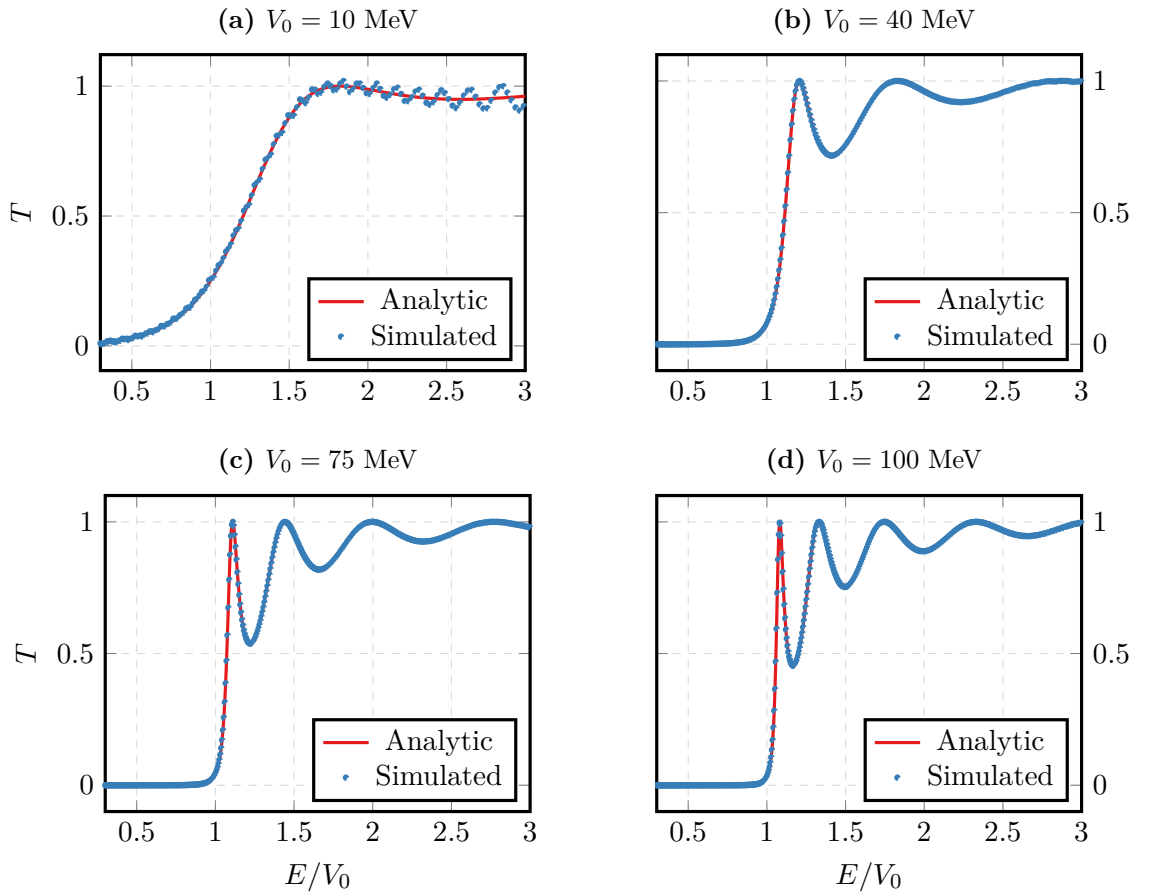
Figure 4.3: Simulated transmission values (points) plotted over analytic transmission curves (solid line) for solutions to the square potential Schrödinger equation.

Table 4.2: Default simulation parameters used in all tests of the algorithmic error. Δt, N and V were varied for each test respectively.

Parameter	Value	Description
N	4096	Number of grid points in each grid
x_{min} (fm)	-500	Minimum point in spacial grid
x_{max} (fm)	500	Maximum point in spacial grid
Δt (fm c^{-1})	0.1	Time step
V (MeV)	40	Barrier height
a (fm)	5	Barrier width
x_i (fm)	-100	Initial wavepacket position
σ_i (fm)	10	Initial wavepacket width
μ (u)	1	Reduced mass

components interacted with the edges of the numerical grid. Both the components inside the barrier and the components at the edge of the grid cause oscillations, which appear in the transmission. Hypothetically, extending the edges of the numerical grid much wider than in this simulation would reduce this by removing the interaction with the boundary, but would not necessarily remove the trapped wavefunction. However, this is not a problem with the numerical functionality of the algorithm, and so will not be discussed further.

The positive results for larger barrier heights, and the general correctness of the shape at $V_0 = 10$ MeV, confirm that the propagation procedure is generally accurate. Continuing with this example, Δx and Δt were varied to find the quantitative dependence of the numerical error, with the purpose to find a combination of step sizes that balances computational speed and accuracy.

4.2.2 Algorithmic contributors to error

In this section I continue with the previous case of a single channel incident on a square barrier. For this, the system was solved for various values of the total time t_f, timestep Δt and grid spacing Δx. The error dependence on these three variables has been characterised using the discrepancy between the computed transmission values and their expected analytic counterparts. The main components of the wavepackets used are at energies near the barrier energy, and so this region is the focus of this error analysis. The default parameters used are recorded in Table 4.2, with one parameter varied in each test.

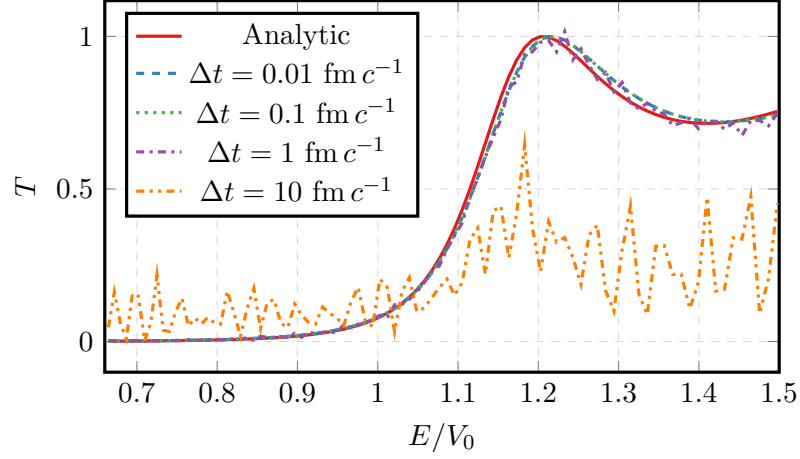The most pure contributor to error is the chosen timestep, as there is no interplay with

Figure 4.4: Transmission probabilities for energies near a barrier $V_0 = 40$ MeV, for several timesteps Δt.

the definition of the reciprocal grid. There should be a clear improvement in the numerical accuracy for smaller timesteps. Initially, timesteps of $\Delta t = 0.01, 0.1, 1.0, 10.0$ fm were chosen and the transmission computed as a function of the energy relative to the barrier. The results for these four timesteps are shown in Figure 4.4. It is at first clear that the largest timestep $\Delta t = 10$ fm c^{-1} is dominated by the additional error introduced, as compared to the smaller timesteps. Removing this result, focus is drawn in Figure 4.5 to a small region, to highlight the discrepancy between the analytic and numerical values. The analytic values in this region are monotonic, and this is matched by the $\Delta t = 0.1, 0.01$ fm c^{-1} plots. The discrepancy between these and the analytic function is explained by the energy grid spacing, which results in an uncertainty in E/V_0 of $\varepsilon_{E/V_0} = 0.02$. Given this result, there is no obvious gain from the smaller timestep of $\Delta t = 0.01$ fm c^{-1} over $\Delta t = 0.1$ fm c^{-1}, and so the latter was used in all future simulations.

Now that a good timestep has been chosen, the error dependence on the grid detail Δx can be analysed. This case will be somewhat different, as increasing the density of points in the position grid improves the application of the potential operator, but also introduces unnecessary points in the k-grid, and increase the Fourier transform error. There is the chance that this error will dominate any improvements in accuracy that the position operator application gains. To evaluate whether this is the case, an examination of a small region is presented in Figure 4.6.

The results of this plot somewhat confirm this hypothesis. All of the Δx considered match the transmission very well below the barrier, where the gradient is small. Above the barrier also matches reasonably well, with the most detailed of the cases, $\Delta x = 0.073$ fm
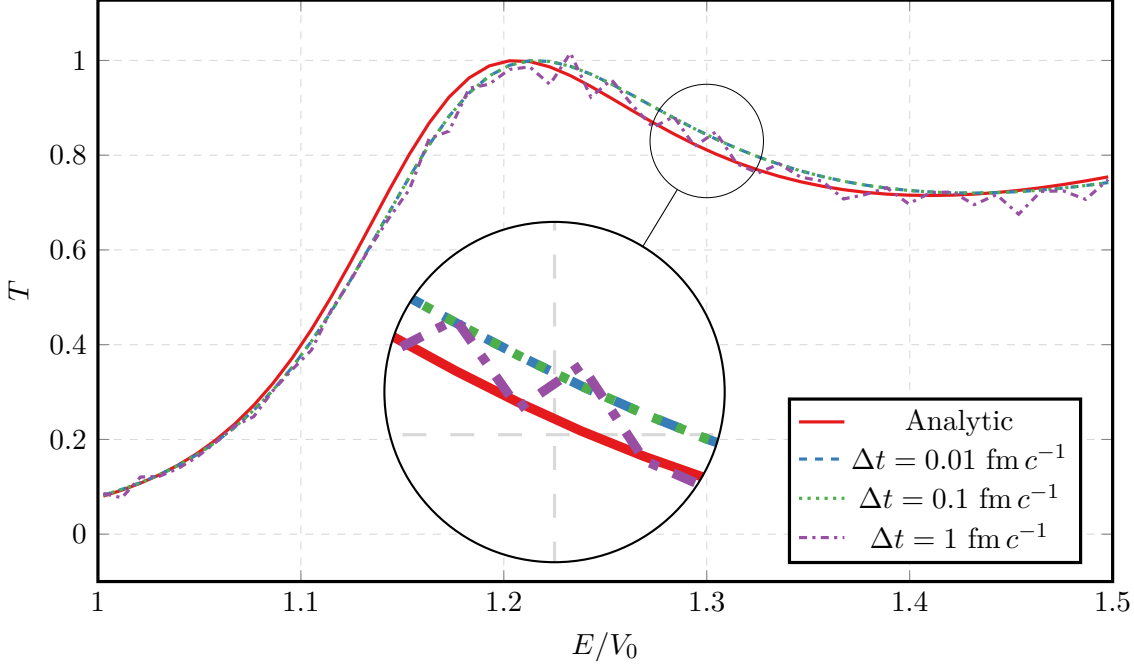
Figure 4.5: Transmission probabilities for energies above a barrier with height $V_0 = 40$ MeV, for several timesteps Δt. A region is magnified to emphasise the matching of the transmission for $t = 0.1$ and $t = 0.01$. The uncertainty in E/V_0 is $\varepsilon_{E/V_0} = 0.02$.
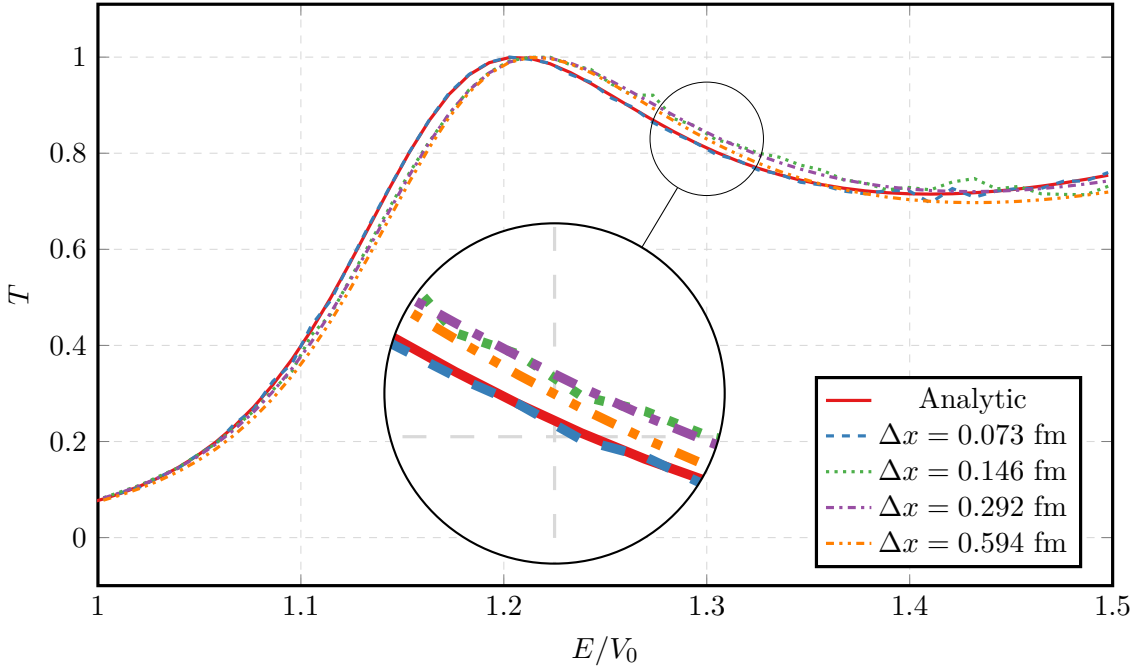

Figure 4.6: Transmission probabilities for energies near a barrier with height $V_0 = 40$ MeV, for several grid steps Δx. A region is magnified to emphasise the accuracy of the most highly detailed grid. The uncertainty in E/V_0 is $\varepsilon_{E/V_0} = 0.02$.
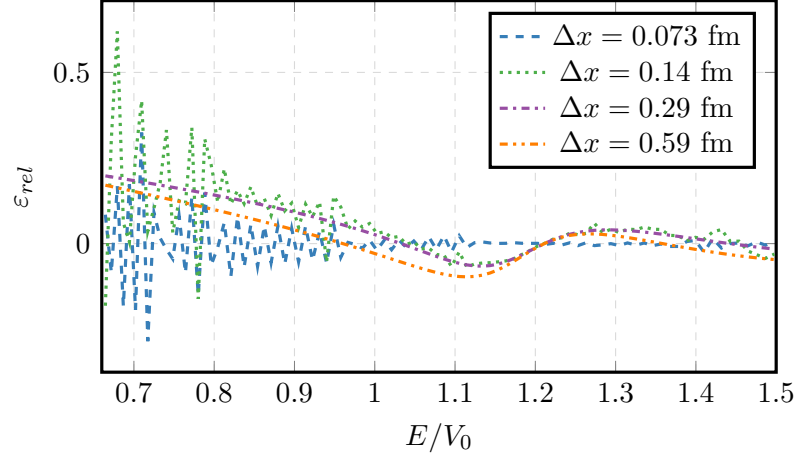
Figure 4.7: Relative errors $\varepsilon_{rel} = (T - T_{An})/T_{An}(x)$ for analytic transmission T_{An} near the barrier energy barrier $V_0 = 40$ MeV, for several grid step sizes Δx.

near exactly matching the analytic curve for all points. The other Δx vary over the transmission curve, where sometimes the most sparse case actually matches the second best. On closer examination, potential numerical effects become evident. While $\Delta x = 0.073$ fm matches the analytic curve best, it and the next most dense, $\Delta x = 0.14$ fm, are less smooth than the larger Δx curves. This becomes more prominent as the energy increases, where artefacts appear most significant in the $\Delta x = 0.14$ fm plot. However, despite these small artefacts, it remains clear that the most detailed grid provides the most accurate transmission curve, with more detail in the representation of the spacial and conjugate grids.

The discrepancy between analytic and simulated transmission can be understood in more detail by looking at the relative error, the percentage difference in the transmission at each energy. As seen in Figure 4.7, the errors for all but the smallest step size have a dependence on the energy, overestimating the transmission below the barrier and underestimating just above the barrier. For $\Delta x = 0.073$ the relative error appears to be randomly distributed, with more significant effects below the barrier where the transmission is smaller.

The potential in this case is discontinuous, and so more prone to numerical difficulties at the edges of the square barrier. The errors at high detail appear to be caused by interaction with this discontinuity, and will likely not be seen for any continuous potential.

Table 4.3: Parameters used to test a two-channel Gaussian barrier system with Gaussian couplings.

Parameter	Value	Description
μ (u)	1	Reduced mass
V (MeV)	10	Gaussian barrier height
σ (fm)	6.0	Barrier width
V_C (MeV)	2	Gaussian ground state coupling height
σ_c (fm)	6.0	Coupling width

4.3 Verification against static coupled channels results

The final tests were performed to verify that the implemented algorithm was accurate for known coupled channels solutions, ensuring that the channel coupling was functional. The first of these tests considered a Gaussian barrier with two channels and a Gaussian coupling, to test the functionality of couplings in Quantum Toolbox. The second test considered coupling between non-degenerate states of a heavier system, to test the non-degenerate coupling and change in mass. The qualitative results of the first case can be seen in Figure 4.8.

4.3.1 A degenerate two-channel system incident on a Gaussian barrier

In this test I considered a Gaussian barrier and wavefunction of the same form as in [3, Sec. 3.1], qualitatively shown in Figure 4.8. In this test there is now an initially unpopulated excited channel at degenerate energy $\epsilon = 0$ which couples to the ground state via a Gaussian coupling potential of height F. The coupling potential and barriers have equal centres $x_0 = 0$ and widths σ and σ_c. The barriers for each channel have equal magnitude V. The values for these parameters are shown in Table 4.3.

The transmission as a function of energy have been presented in Figure 4.9. Simulated values using Quantum Toolbox successfully reproduce the results in [3], depicting enhanced transmission below the barrier, and an equal suppression above the barrier, due to the presence of the coupling. The coupling changes the inflection point at the barrier height of $V = 10$ MeV, creating instead two inflection points at $V \pm F$ MeV.

This demonstrates the potential effect of the coupling. Even for degenerate energy channels, just the presence of a coupling potential during interaction with a barrier can drastically alter the transmission probability. However, it is not systematically clear how
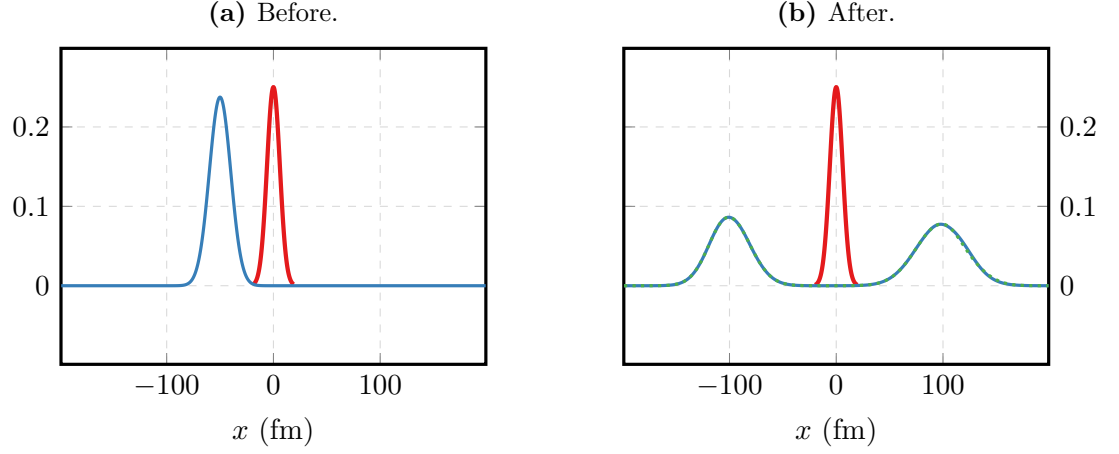
Figure 4.8: Gaussian wave-packet tunnelling through a Gaussian barrier with one coupling. Initially in the ground state (solid), it partially tunnels, with half the wavefunction magnitude moving into the excited channel (dashed), overlapping with the ground state channel.
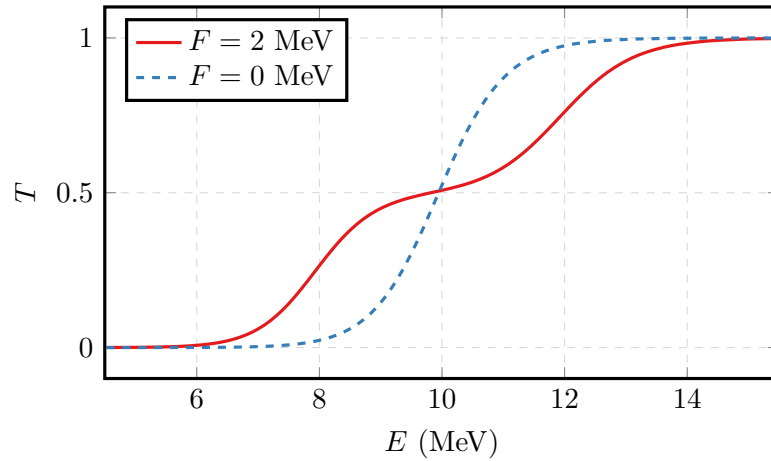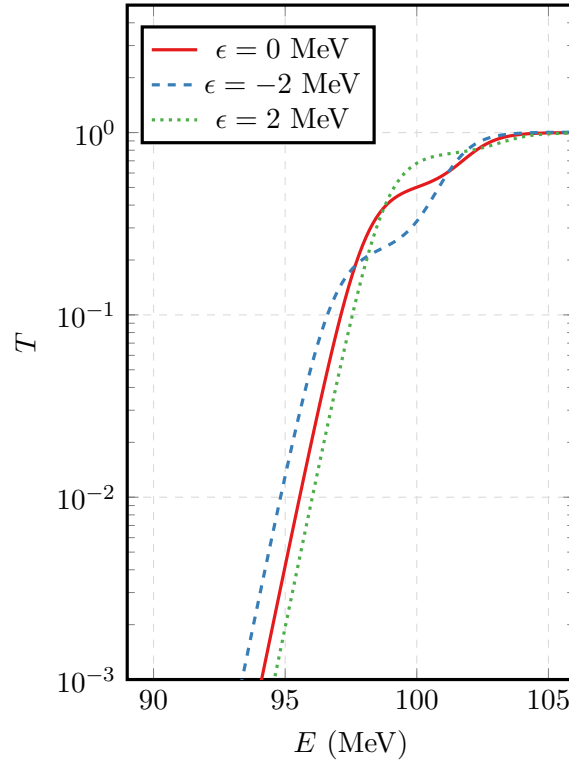

Figure 4.9: Transmission probabilities for a range of energies incident on a 10 MeV Gaussian barrier, for a degenerate two-channel system with a Gaussian coupling potential of height $F = 2$ MeV. The uncoupled case of $F = 0$ MeV has also been calculated for comparison.

this altered transmission probability depends on the number, strengths and locations of the couplings, nor how the states are connected.

The functionality of multiple channels and couplings in Quantum Toolbox has been confirmed by this test. The final pieces of functionality that need to be shown are non-unit reduced mass systems, and non-degenerate channel energies.

4.3.2 A non-degenerate two-channel system incident on a Gaussian barrier

Non-degenerate channel energies are the most common types of reaction channels, representing the excited states of the projectile and target nuclei , as well as nucleon transfer states. In a reaction, some of the wavefunction may couple into these channels, in which the kinetic energy is modified. This means that the final wavenumber, and thus final energy state, is actually different for these channels compared to those matching the energy of the ground state. This requires a modification to the calculation of the transmission coefficients. Thus, to calculate the transmission for an ground state energy $E(k)$, the function becomes

$$T_{E(k)} = \sum_n \frac{\left|\psi_f^n(k_n)\right|^2}{\left|\psi_i^0(k)\right|^2}; \qquad\qquad k_n = \frac{\sqrt{2\mu\left(E(k) - \epsilon_n\right)}}{\hbar} \qquad\qquad (4.5)$$

where the wavefunction is entirely in the initial state of the ground channel ψ_i^0, and ends up spread across the final states of all channels ψ_f^n, each of which have an energy ϵ_n less than the degenerate energy. In practice, to match the correct k_n for the gridpoints k, the magnitudes of the closest wavenumbers need to be found, and interpolated between. The increased mass of a system reduces the wavepacket velocity, requiring an increased simulation time to reach the asymptotic region in which the potential is negligible and the transmission can be computed. It also increases the maximum possible wavenumber, and so requires the spacial grid endpoints to be narrowed to maintain resolution in k and E.

The test the functionality of Quantum Toolbox with both non-degenerate energies and non-unit masses, I considered a Gaussian barrier and wavefunction of the same form as in the paper by Dasso *et al.* [3, Sec. 3.2, Fig. 8]. In this test, a wavepacket of mass μ is incident on a Gaussian barrier of height V, and Gaussian coupling potential height V_C, with equal widths $\sigma = \sigma_c$. The simulation was run for an excited state with relative energies of $\epsilon = -2, 2$, and compared to the degenerate energy case $\epsilon = 0$.

Table 4.4: Parameters used to test a non-degenerate two-channel Gaussian barrier system with Gaussian couplings.

Parameter	Value	Description
μ (u)	29	Reduced mass
V (MeV)	100	Gaussian barrier height
σ (fm)	3.0	Barrier width
V_C (MeV)	2	Gaussian ground state coupling height
σ_c (fm)	3.0	Coupling width

Figure 4.10: Transmission probabilities for a range of energies incident on a 100 MeV Gaussian barrier, for a two-channel system with a Gaussian coupling potential of height $F = 2$ MeV and excited state relative energies of $\epsilon = -2, 0, 2$.

The transmissions for this case at near barrier energies are shown in Figure 4.10. This also exactly matches the result in Dasso *et al.*, and also the same configuration, instead with degenerate energies and modified barrier heights.

As well as being a good test, this case demonstrates that positive ϵ, while suppressing fusion far below the barrier actually enhance fusion rates at near barrier energies with respect to degenerate channels. The opposite effect is seen for negative ϵ, which sees significant suppression at near barrier energies.

Exploring dissipation with time-dependent coupled channels

Now that the efficacy of Quantum Toolbox and its time-dependent coupled channels solver has been proven, it can be used to investigate open problems in nuclear reactions. There are many interesting aspects of time-dependence in nuclear collisions, particularly that of coupling and its influence on tunnelling and fusion. In fact, time-dependent coupled channels can likely be used successfully in every case that time-independent coupled channels has been, potentially deriving more interesting results from the intermediate non-stationary states and their evolution. However, the focus of this thesis is on the two key problems identified earlier; dissipation leading to reduced fusion rates which is unidentified in static coupled channels; and consistent treatment of the time-dependent and dissipative nature of fusion itself. Preliminary investigation of both is presented in this chapter. The paths followed in these investigations were suggested by my supervisor, and the the rest is my own work.

5.1 Setting the scene for dissipation

The locations of dissipation and fusion can be matched to the two salient features of the combined nuclear and Coulomb potential shown in Figure 5.1; the potential pocket (**A**) and the fusion barrier (**B**) respectively. For dissipation, the observed losses are likely due to higher order coupling due to nucleon and energy transfer between the nuclei, which can only happen within the range of the nuclear potential. The reduction of fusion must result in increased reflection, and so the leading edge and peak of the fusion barrier are likely the main stage on which this occurs. Since the purely Coulomb tail doesn't impinge on this, as a first approximation it can be ignored, meaning the fusion barrier closely resembles a Gaussian form. This will allow for very low energy interaction with the barrier region
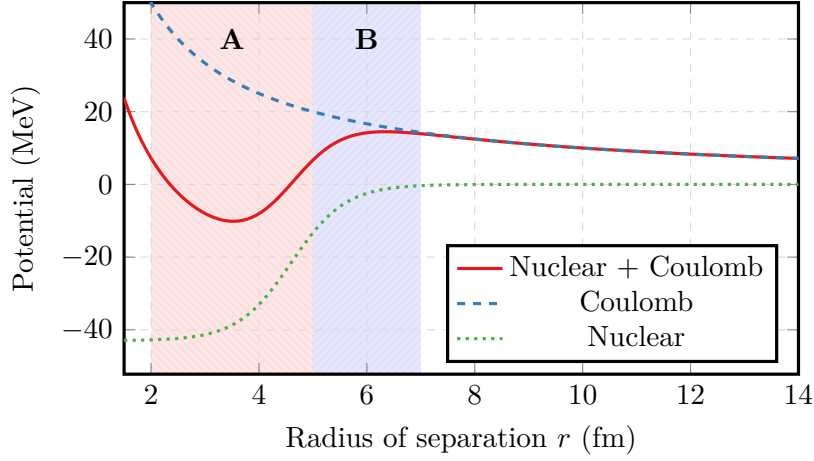
Figure 5.1: An example of the nuclear and Coulomb potentials, identifying the potential pocket (**A**) and the fusion barrier region (**B**).

than with the Coulomb tail, which can generally be ignored for this study. It is this form for the barrier that will be used to study dissipation in Section .

Fusion itself is highly dissipative, involving a multitude of complicated couplings at short distances. A uniquely time-dependent way to include fusion is to describe it as higher order coupling inside the potential pocket. Higher order states will see a higher effective barrier due to their positive ϵ, and so remain trapped inside the potential pocket. Coupling back down to lower states will allow the wavefunction to eventually fully tunnel back out of the pocket. The time-dependence of this trapping means that this treatment of fusion could not be used with static coupled channels. The first test of this explanation is to show it is possible for most of the wavefunction to move into higher order states, and then return back to the ground state, on timescale similar to those seen for fusion. A parabolic potential will therefore be used to study this trapping in Section 5.3.

5.2　Gaussian coupling potentials in a Gaussian barrier

One of the key problems faced by coupled channels approaches is the set of required inputs. These include the exact form of the effective potential for which the Woods-Saxon component is likely problematic. They also include the potential states of the two-ion system, such as rotational and internally excited states, with their associated energy differentials. However, the most problematic input is the form of the couplings, the off-diagonal potential terms which couple different states of the two-particle system to each other. Those important to the dissipation problem appear to relate to inelastic

Table 5.1: Default simulation parameters used in all dissipation tests. x_0, σ_c and V_C were varied for each test respectively.

Parameter	Value	Description
V (MeV)	100	Gaussian barrier height
σ (fm)	5.0	Barrier width
V_C (MeV)	4	Gaussian ground state coupling height
x_0 (fm)	0.0	Coupling centre
σ_c (fm)	5.0	Coupling width

and deep-inelastic scattering, where the ions lose energy through the strong interaction, occasionally including nucleon transfer. This is a short-range interaction, and so will occur near the fusion barrier peak (shown back in Chapter 2, Figure 2.1), in the same region as the Woods-Saxon potential.

A Gaussian form for a potential acts as a substitute for this fusion barrier without the potential pocket. The coupling potential in this same region, however, is less well understood. In these studies the effects of the coupling potentials were examined. They were then varied in form relative to the barrier centred at the origin, with the goal of qualitatively understanding the effect of these changes on macroscopic results.

In all cases, the same scenario was run for $N \in \{1, 2, 3, 4\}$ channels following the coupling scheme presented in Figure **??**. For each channel, the relative energy of each level $n \in \{1, \ldots, N\}$, and the coupling strength V_C, scale with n. For each n, the energy of that level $\epsilon_n = n\epsilon$, and the coupling height to the next level $V_{n \to n+1} = V_{n+1 \to n} = nV_C$ for baseline multipliers ϵ and V_C shown in Table 5.1. This can be qualitatively understood as a linear "ladder" coupling scheme, chosen to simulate the increasing energies of the states, and the fact that for physical systems they increase in density, and thus should be simpler to transition between.

5.2.1 Standard calculation

As an exploratory analysis of the form of the coupling and its impact on dissipation, it helps to build a systematic understanding of the results of coupling. To do this, I first examined a control system with a moderate coupling height V_C centred inside the Gaussian potential at $x_0 = 0$. The transmission shown in Figure 5.3 demonstrates additional turning points for two channels, as seen in the previous chapter. As further channels are included this appears to flatten the transmission curve, showing a non-trivial dependence on the
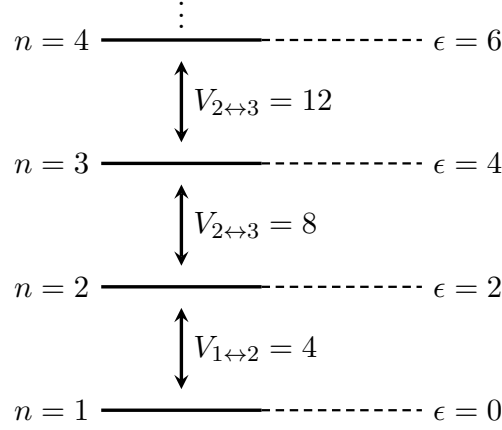
Figure 5.2: Level diagram for the linear coupling scheme and channels used for this dissipation study.
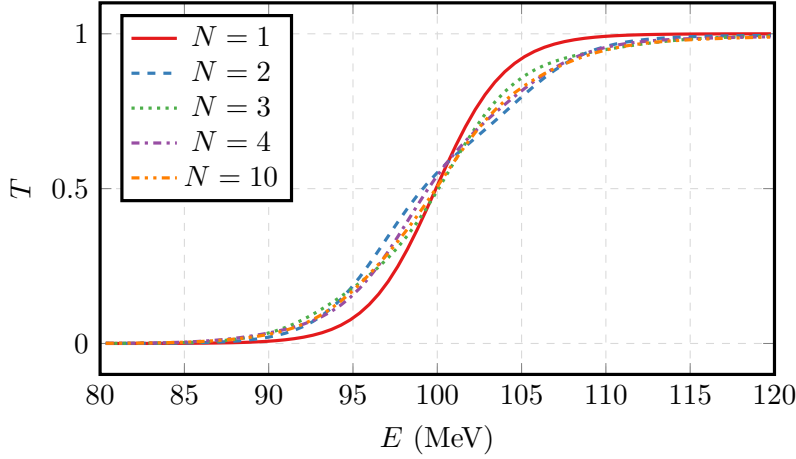

Figure 5.3: Transmission probabilities for a range of energies and $N \in \{1, \dots, 4\}$ channels, for a control coupling potential of height $V_{n \to n+1} = 4n$ MeV, centre $x_0 = 0$ fm and width $\sigma_c = 5$ fm. The many channel case $N = 10$ has been included to exhibit limiting behaviour.

number of channels.

Looking at the low energies in more detail, it can be seen that additional couplings act to enhance the transmission compared to the uncoupled case, as shown in Figure 5.4. This highlights that the couplings enhance tunnelling at low energies, with more complex interactions arising at near barrier energies around 90% of the barrier height of 100 MeV. That the couplings enhance sub-barrier fusion, and that more couplings enhance it more is not surprising, but verifies that the chosen coupling scheme performs sensibly.

The above barrier behaviour is more interesting. In the uncoupled case the transmission rapidly approaches $T = 1$ and doesn't drop below this value for energies within the range where the calculations are accurate. However, the coupled systems exhibit a damping of this behaviour, instead slowly converging towards $T = 1$ for increasing energies.
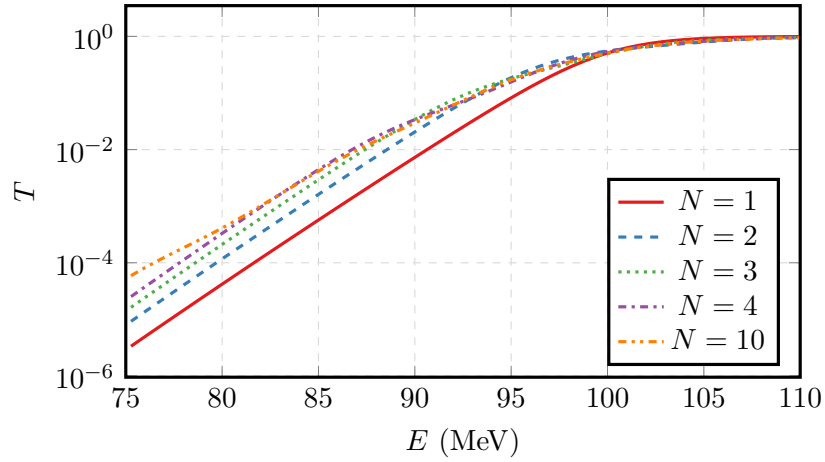
Figure 5.4: Low energy transmission for the control case shown in Figure 5.3.
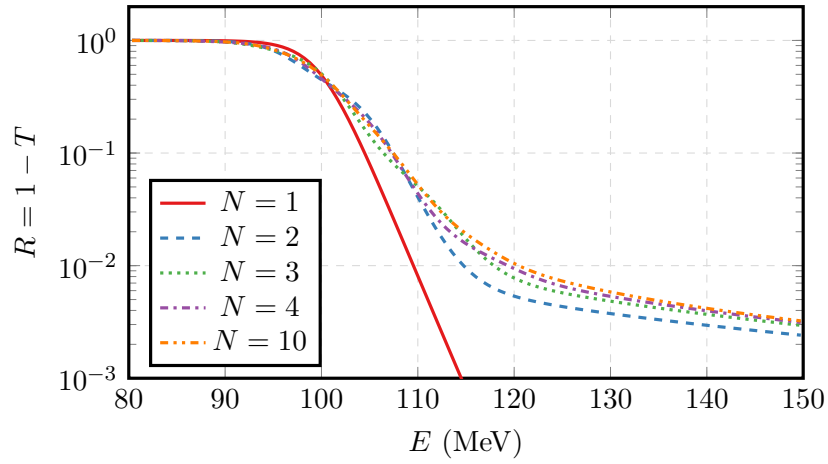
Figure 5.5: A graph of the reflected flux $R = 1 - T$ highlighting the high energy transmission for the control case shown in Figure 5.3.

The underlying reason for this is unclear from the transmission curve, and so it helps to examine the population of the different channels over time, as compared to the uncoupled case.

In Figure 5.6 the reflected components of each channel at $E = 120$ MeV are shown, an energy within the region of interest. The reflected components show a dramatic increase as the system initially interacts with the barrier, and then a plateau once this interaction is complete. Importantly, it highlights an effect seen in all coupled cases; each component appears to be reflected similarly to the uncoupled case, meaning the overall reflection is enhanced and the transmission is damped. However, examining the behaviour of the reflection for various energies above the barrier gives no indication that this damped transmission should be dependent on the energy.

The reflection as a function of energy also provides some insight into the near-barrier
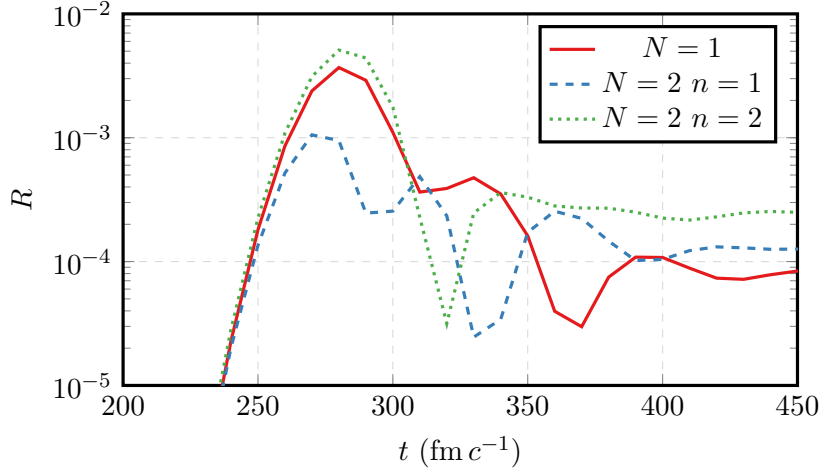
Figure 5.6: The magnitude of the reflected wavefunction components with $E = 120$ MeV over the time of the interaction.
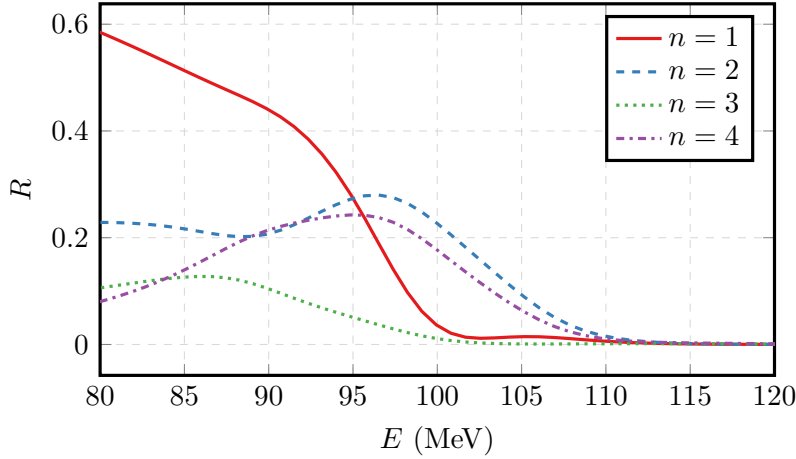
Figure 5.7: Reflection probabilities decomposed into the component channels for the $N = 4$ control case.

behaviour. In Figure 5.7, the components of the reflection as a function of the energy are shown. As is expected, the reflection magnitude is near unity for low energies. As the energy increases, more of the wavefunction is able to tunnel or pass a portion of the barrier, and begins interacting with the coupling potential. The first excited state becomes populated, and some of this population can be coupled into the next excited state. This low energy behaviour is overemphasised For high enough energies the wavefunction is exposed to the coupling enough that the first excited state actually reduces in magnitude, as it has had time to drain into the higher order couplings.

This gives some indication that the timing of the coupling is important in describing dissipation, as there must be enough interaction to populate the higher order states which reduce the fusion rate at higher energies.

A perhaps more valuable tool than the transmission and reflection curves is the so-called "barrier distribution". This curve, the derivative of the transmission, is most commonly derived from the energy dependence of the experimental cross section [66]. It allows a visualisation of the effective barrier the total system experiences.

As a very brief introduction to the barrier distribution, consider the difference between a classical and quantum system incident on a step potential. The classical system cannot pass unless its energy is high enough, and if so it will all pass the potential, giving it a step function transmission at the potential height. For the quantum system, some tunnelling occurs, smoothing the transmission around this energy by reducing the high energy transmission and increasing the low energy transmission. Considering the derivatives of these two transmissions, the classical system will have a delta function at the step potential energy, and the quantum system will have a distribution around this energy. This describes the barrier distribution the quantum system encountered.

The barrier distribution for all cases is dependent on the number of channels, their energy, and their coupling strengths. For the control case, Figure 5.8 presents a single barrier at 100 MeV for a single channel, identical to the input. For two channels the barrier splits into the sum of two barriers. This trend continues, with the $N = 4$ case having a small fourth barrier near 135 MeV.

The locations of these barriers can be somewhat explained by the eigenvalues of the potential matrix. For example, the $N = 3$ case the potential matrix in the state basis can be approximately diagonalised as

$$V = \begin{bmatrix} 100 & 4 & 0 \\ 4 & 100 & 8 \\ 0 & 8 & 100 \end{bmatrix} \rightarrow D = \begin{bmatrix} 100 & 0 & 0 \\ 0 & 91 & 0 \\ 0 & 0 & 109 \end{bmatrix} \tag{5.1}$$

which can be interpreted as the effective barriers in some uncoupled basis. The results are in reality also dependent on the energies of the channels, and the exact timing of interaction with the coupling potentials changing the relative magnitudes. This is why the apparent locations of the barriers for this case appear to be closer to 94, 102 and 112 MeV. However, this at least gives an indication that the shift of the barrier locations relative to the eigenvalues may be of the same order as the channel internal energy ϵ. Eigenvalues for each number of channels N for the control case are presented in Table 5.2.

The higher energy components of the barrier distribution further reveal why the cou-

Table 5.2: Default simulation parameters used in all dissipation tests. x_0, σ_c and V_C were varied for each test respectively.

Parameter	Value	Description
V (MeV)	100	Gaussian barrier height
σ (fm)	5.0	Barrier width
V_C (MeV)	4	Gaussian ground state coupling height
x_0 (fm)	0.0	Coupling centre
σ_c (fm)	5.0	Coupling width
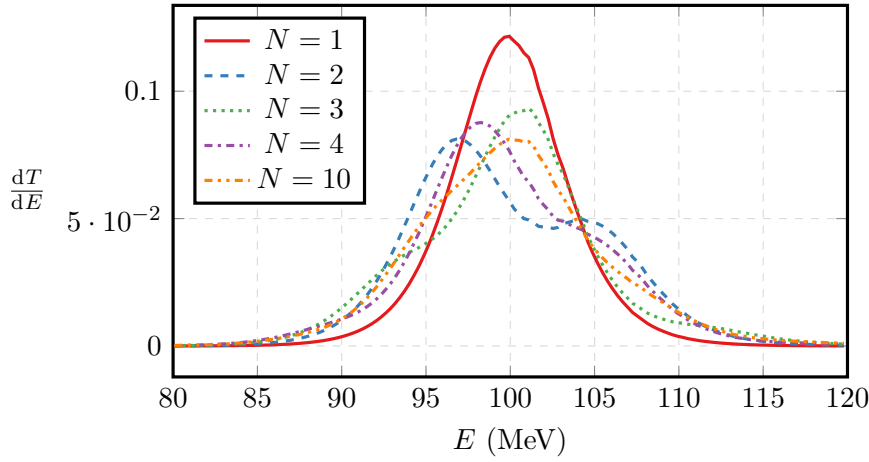
Figure 5.8: Barrier distributions for the control case. The kink slightly above the barrier height of 100 MeV appears to be a numerical artefact.
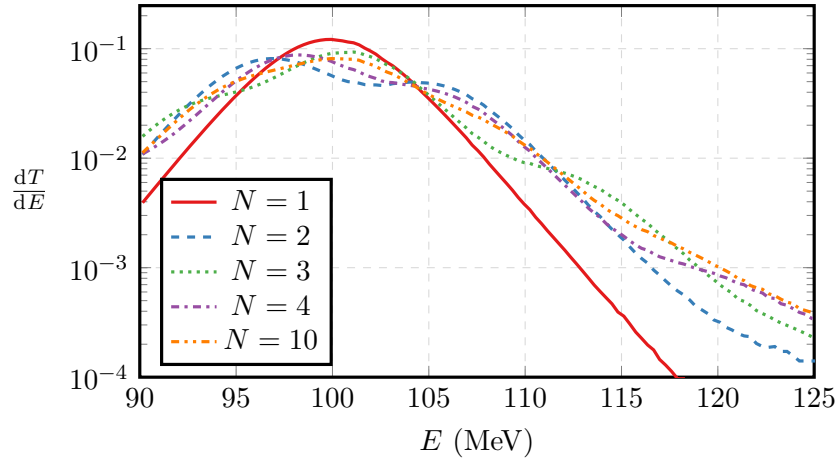
Figure 5.9: Higher energy components of the control case barrier distribution.

pling damps transmission at higher energies. The multiple effective barriers spread the distribution, and so the coupled cases experience a much stronger barrier at higher energies than the uncoupled case.

5.2.2   Stronger couplings

Now that the general properties of the uncoupled and coupled cases have been identified for this example, it is interesting to see whether these properties change for variations in the coupling form, and whether this gives any further indications about dissipation.

In this first variation, the height of the Gaussian coupling potential was doubled for all channels. The first change in the transmission, shown in Figure 5.10, is the general enhancement of the coupling effects. In the transmission the general flattening behaviour is still seen for increasing N, but the turning points associated with each channel are much more influential for this stronger coupling.

In Figure 5.11 the low energy transmission shows a spreading of the near barrier behaviour to lower energies. The below barrier enhancement due to coupling is significantly increased by the stronger coupling. These interactions are also spread to higher energies, shown in Figure 5.12.

The source of this spreading can be seen in the barrier distribution in Figure 5.13, for which the increased coupling strength has spread the component barriers further apart.

This spread can be further understood by examining the reflected wavefunction density, shown in Figure 5.14. As the coupling height has increased, its width has also increased. For an energy that makes it into the barrier region, the doubled coupling strength acts more dramatically than the control case. In addition, the increased width means it will impact
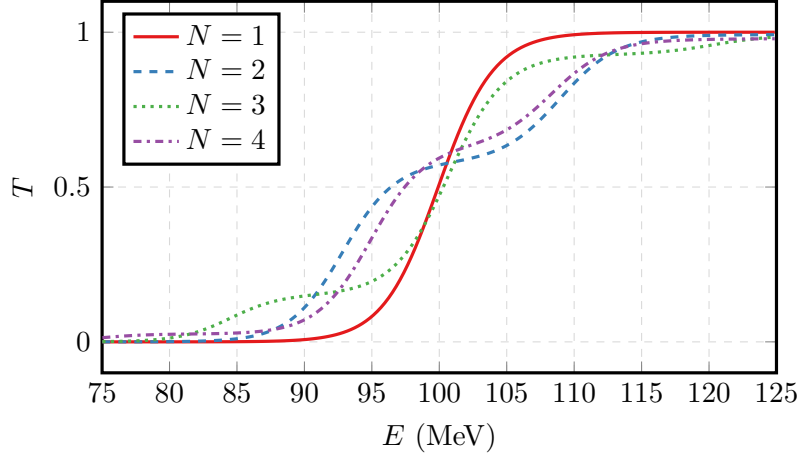
Figure 5.10: Transmission probabilities for a range of energies and $N \in \{1, \dots, 4\}$ channels, for an increased coupling potential of height $V_{n \to n+1} = 8n$ MeV, centre $x_0 = 0$ fm and width $\sigma_c = 5$ fm. The integral of the coupling potential is not maintained relative to the control.
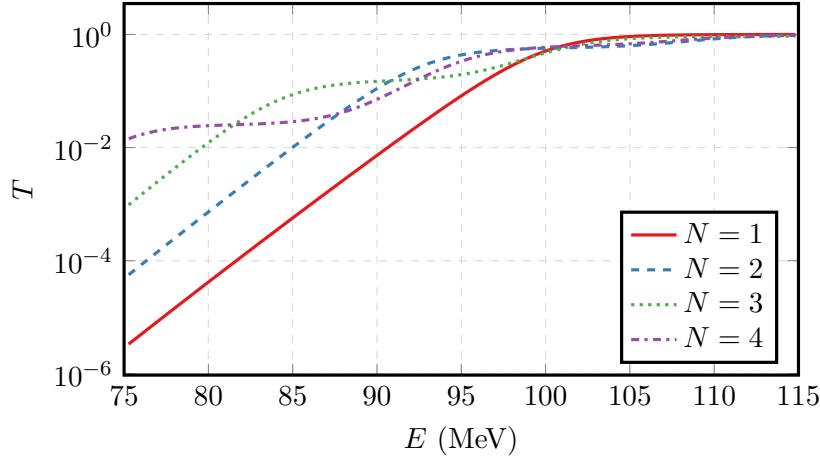

Figure 5.11: Low energy transmission for the doubled coupling potential height shown in Figure 5.10.
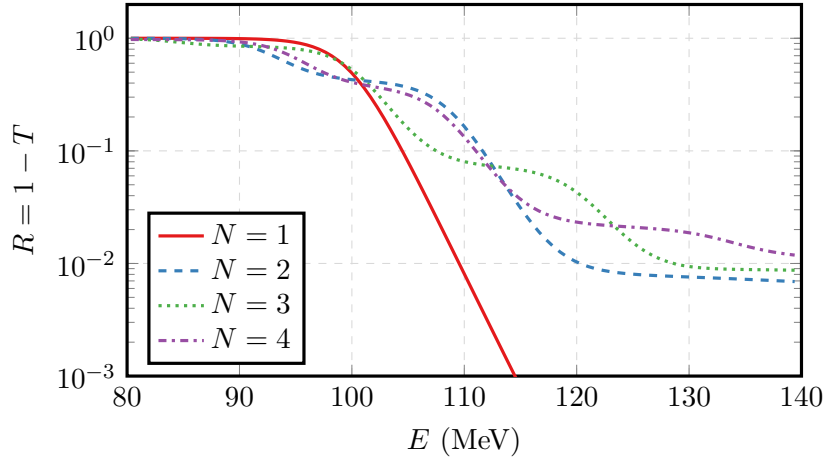

Figure 5.12: A graph of $R = 1 - T$ highlighting the high energy transmission for the doubled coupling potential height shown in Figure 5.10.
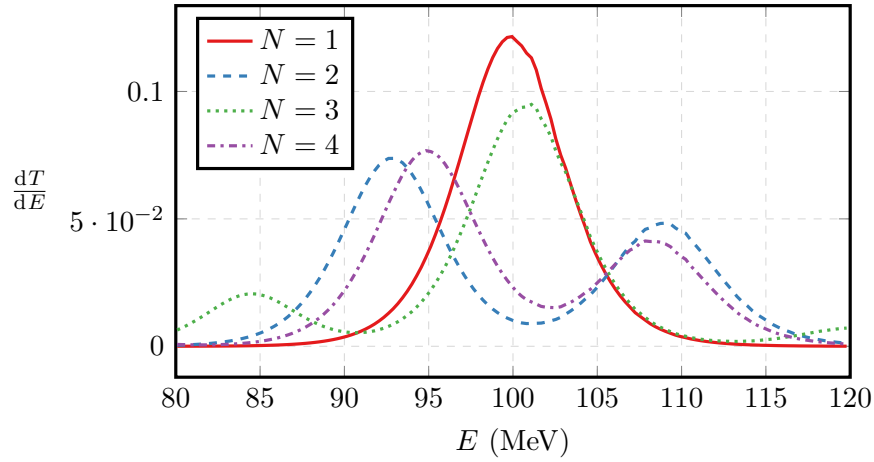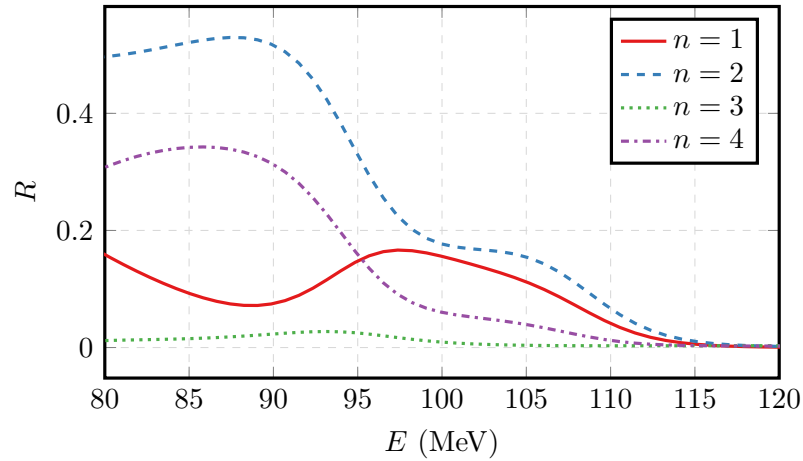
Figure 5.13: Barrier distributions for the doubled coupling potential height.

Figure 5.14: Reflection probabilities decomposed into the component channels n for $N = 4$ channels with doubled coupling height.

lower energy components than the control. This heightens the excited state reflections and shifts their peaks to a lower energy.

5.2.3   Leading edge dissipation

To characterise the separate influence of this lower energy interaction, the control potential was shifted forward by half of the width at half maximum. This will emphasise any effect derived from the leading edge of the heightened coupling, without also including its impact in the barrier region centre.

The transmission (shown in full in Figure 5.15) in this case is reduced above barrier (Figure 5.17) without a significant enhancement below the barrier (Figure 5.16). This is exactly the type of dissipative behaviour expected of heavy systems, where the longer range potential (in this case shifted forwards) results in transmissions similar below barrier,
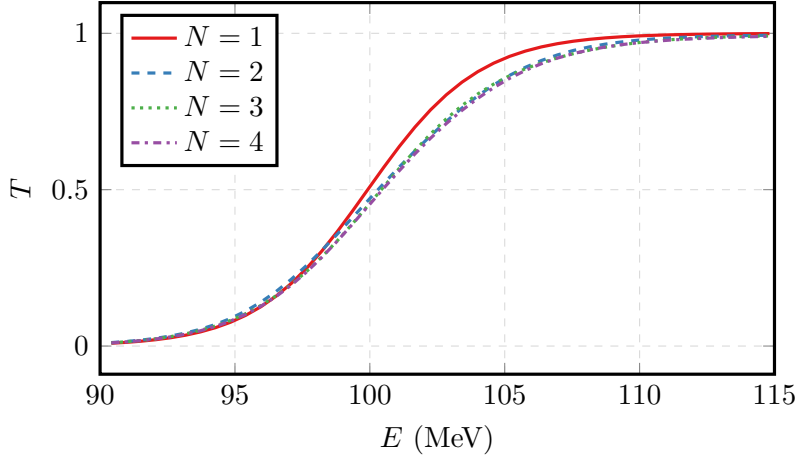
Figure 5.15: Transmission probabilities for a range of energies and $N \in \{1, \ldots, 4\}$ channels, for forward shifted coupling potential of height $V_{n \to n+1} = 4n$ MeV, centre shifted to the left of the full width at half maximum $x_0 = -5\sqrt{2 \ln(2)}$ fm and width $\sigma_c = 5$ fm. The integral of the coupling potential is conserved relative to the control.

but reduced above barrier relative to a single tunnelling state. In this case it is shown to occur through coupling to higher energy states, which means kinetic energy is lost to the internal state and the barrier becomes relatively higher for these components of the wavefunction.

This can also be seen in the barrier distribution, Figure 5.18, which remains centred at 100 MeV and matches the uncoupled case for low energies, but exhibits a tail for higher energies. The form of the barrier distribution matches the uncoupled case below the barrier, is reduced near the barrier, and increased above the barrier.

5.2.4 Evidence of dissipation

Several aspects of the coupling form have been identified as important in describing dissipation. The first is the inclusion of several levels of coupled states, which damps the transmission probability at above barrier energies. The second is the position of the barrier, which when shifted forward emphasises this damping. In reality, it is likely there are multiple stages of coupling. Some coupling at the forward edge of the barrier with small ϵ would describe inelastic scattering states, with a second set of couplings deeper into the barrier describing higher ϵ states related to deep-inelastic processes such as nucleon transfer. Such a combination is beyond the scope of this thesis, but would amplify the perceived dissipation at higher energies relative to a minimally coupled case.
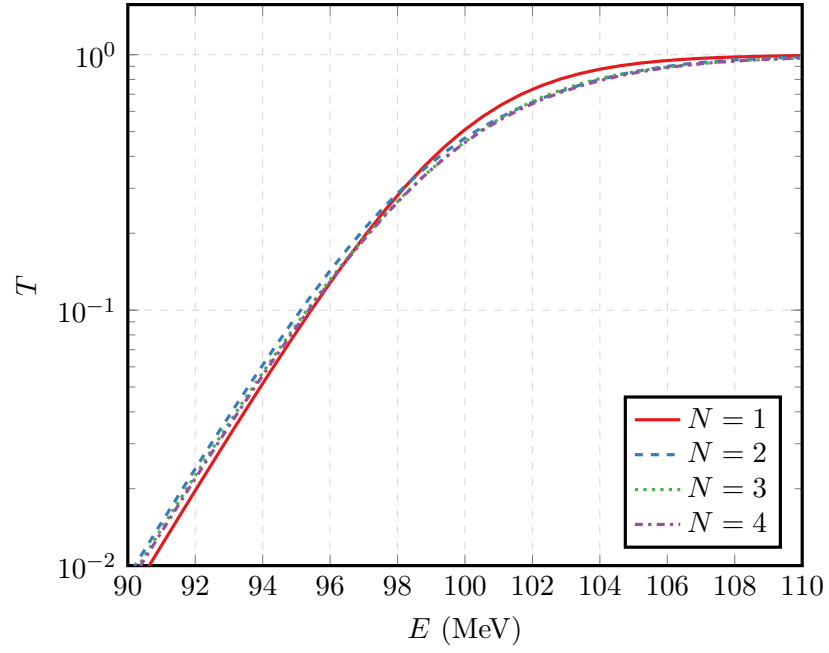
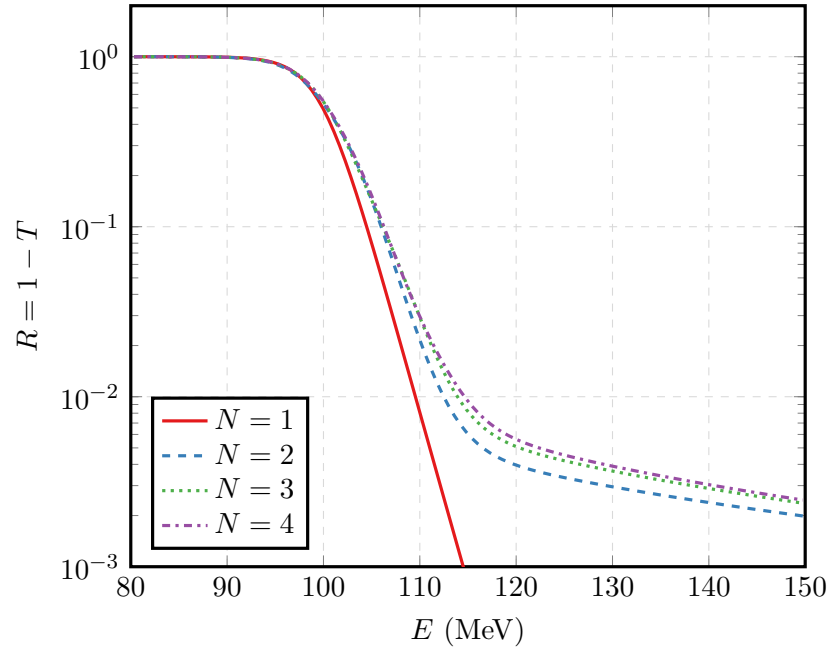Figure 5.16: Low energy transmission for the shifted coupling potential shown in Figure 5.15.

Figure 5.17: A graph of the reflected wavefunction $R = 1 - T$ highlighting the high energy transmission for the shifted coupling potential shown in Figure 5.15.
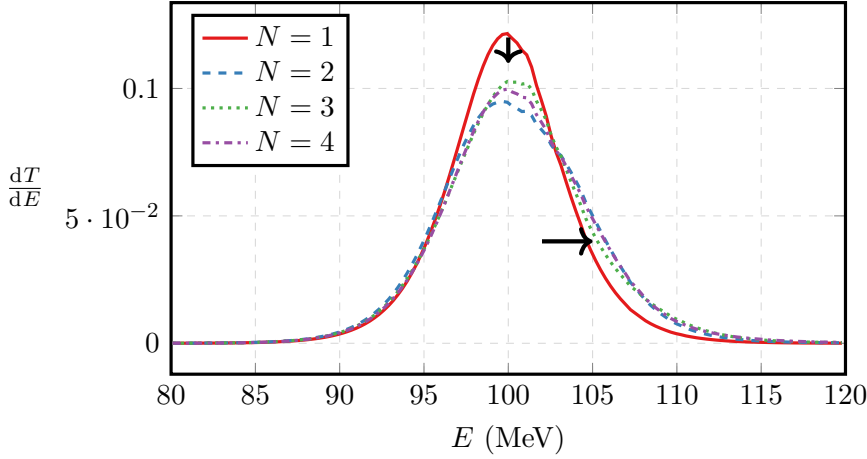
Figure 5.18: Barrier distributions for the shifted coupling potential.

5.3 Trapping through coupling as a mechanism for fusion

As well as early in reactions, before fusion occurs, dissipation is inherent to the fusion process itself. One of the issues identified with time-independent coupled channels is the use of artificial boundary conditions to simulate fusion. In reality, fusion is a time-sensitive process, with fused products existing for approximately 10^{-18} s, or about 300000 fm c^{-1} before any emission of nucleons occurs. A time-dependent approach allows for a new, more physical description of fusion; dissipation into higher order channels inside the barrier region. This dissipation should act in a similar way to that before the barrier, reducing the transmission of the wavefunction through the potential. The difference in this case is that it will act to trap the wavefunction inside the barrier, rather than preventing it from entering in the first place. In this section we explore this possibility.

5.3.1 Studies of ground state recurrence in a parabolic potential

Potentials with walled regions, such as a square potential with an infinite wall, admit resonant solutions which can become stuck inside the walled region [59]. This is hypothetically also possible for the potential pocket, shown in Figure 5.1, and would be more likely for large ϵ excited states which experienced a heightened effective potential at the fusion barrier, which would reduce the rate at which the wavefunction escapes. The transmitted coefficients could then be calculated from the reflected flux as a function of time.

To investigate whether this description is possible, a ground state "recurrence time" was the key identifier of success. Such a recurrence time, the time between peak population in the ground state, would describe a temporary dissipation of the wavefunction into higher
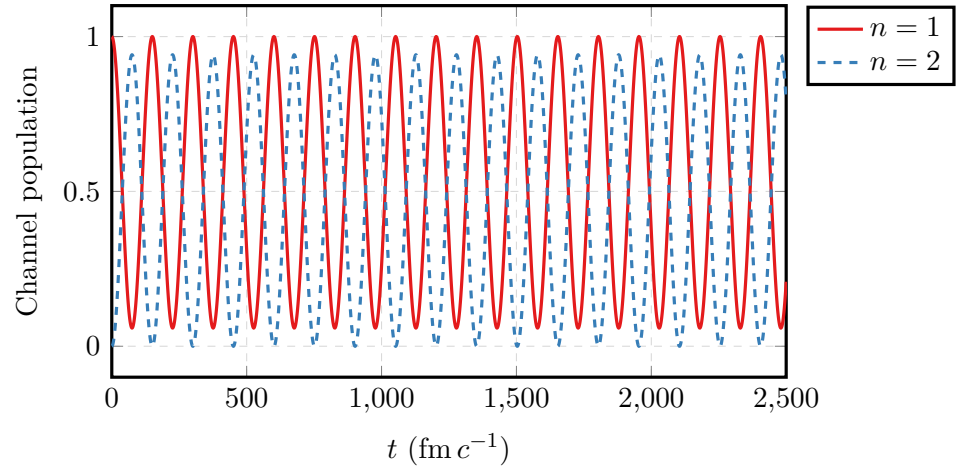
Figure 5.19: Channel populations overtime for a two level system.

order states, a potential descriptor for fusion. The first set of cases were for the same "ladder" coupling scheme as earlier, with constant coupling potentials for the whole grid.

Keeping in mind that the timescale of the simulations is in $\mathrm{fm}\,c^{-1}$, for which 1000 $\mathrm{fm}\,c^{-1}$ is approximately 3 zs. The zeptosecond is approximately the timescale of nuclear reactions, and so a significant enough recurrence time to simulate fusion needs to be on the order of 1000 $\mathrm{fm}\,c^{-1}$.

Starting with a two-channel case, there is a clear recurrence time of approximately 150 $\mathrm{fm}\,c^{-1}$.

As the number of channels is increased, this oscillation becomes less clear as the couplings interact. However, out of this interaction comes an interesting global behaviour. As shown in 5.20, the fast oscillations remain somewhat intact for many couplings. In addition, there appears to be a global slow oscillation in the ground state on the order of approximately 1200 $\mathrm{fm}\,c^{-1}$.

The dependence of this recurrence on the couplings can be further understood by instead doubling the coupling strength as you move up in excitation energy, as opposed to linearly increasing coupling strengths. In this case, the period of the recurrence for the two channel case is halved, as the wavefunction density is moved twice as fast between the two channels. A similar slow phase in the ground state can be seen for many channels, for example a seven channel system in Figure 5.21.

There appears to be a strong dependence on the coupling scheme in this case, as for doubling coupling strengths the global slow oscillations only appear clearly for an odd number of couplings. The coupling scheme used in these cases has been linear, with states only connected to at most two other states in a "ladder" scheme, as seen in Figure **??**. As
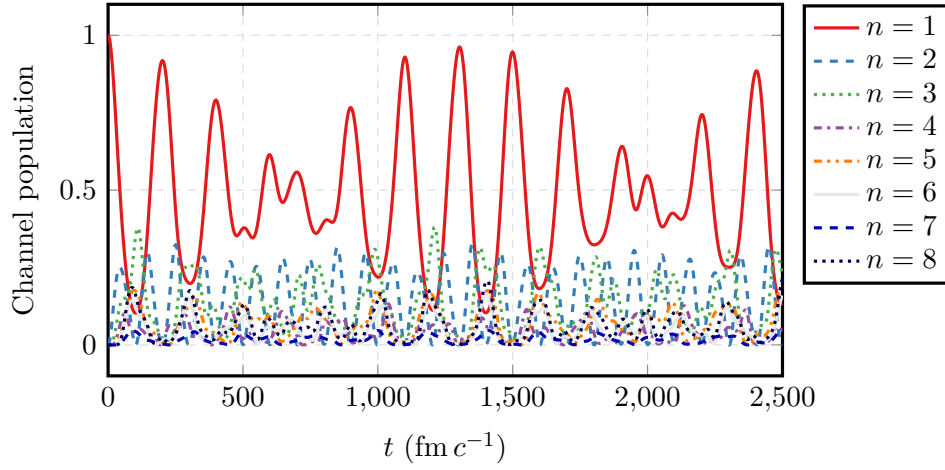
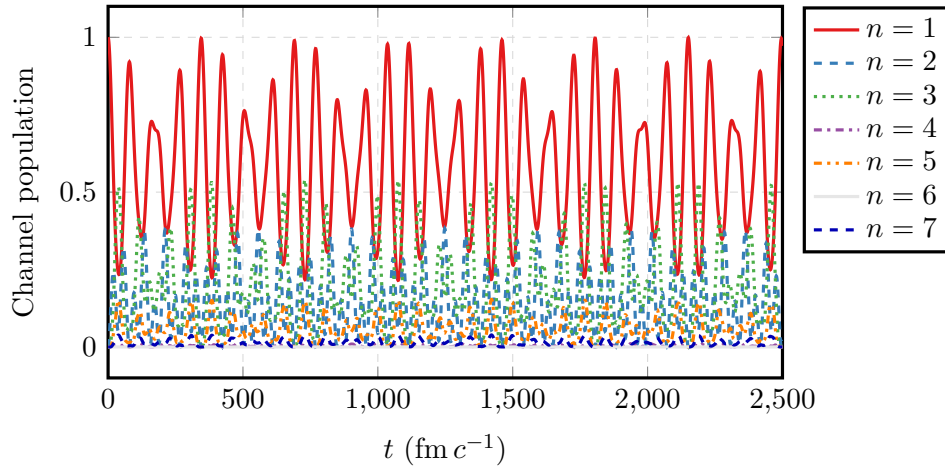Figure 5.20: Channel populations overtime for an eight level system.

Figure 5.21: Channel populations overtime for a seven level system with doubling coupling strengths.
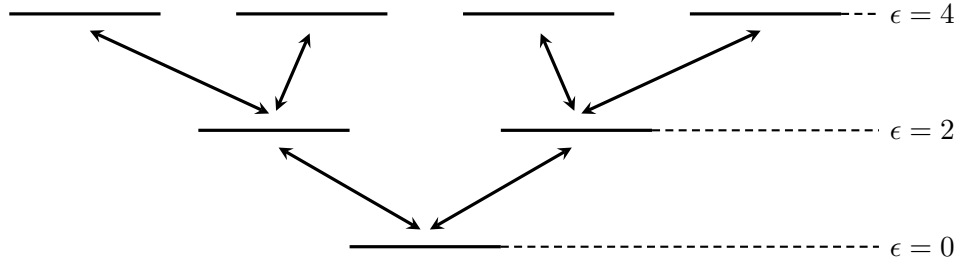
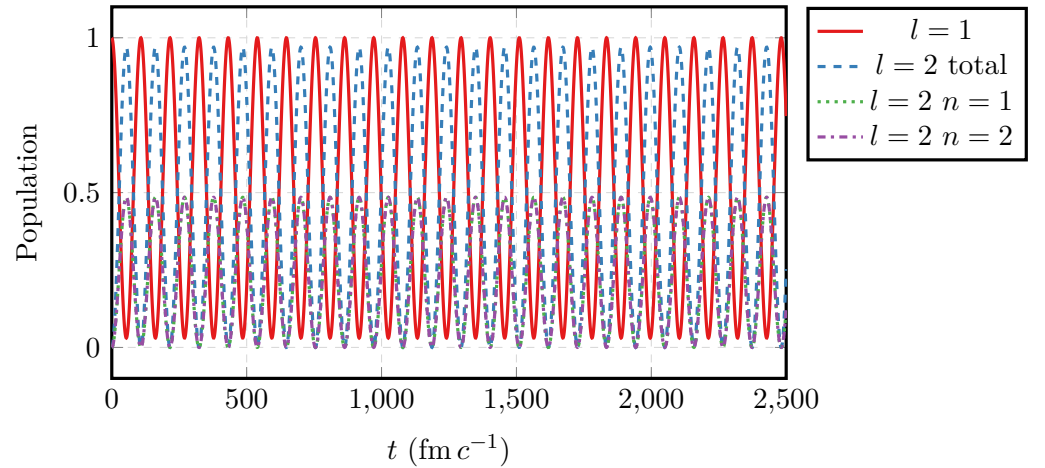Figure 5.22: Level diagram for the tree coupling scheme.

Figure 5.23: Channel and level populations overtime for a two level tree.

the number of couplings are small relative to the number of states, it is highly likely that much of the behaviour seen is a result of symmetries in this scheme. To check whether this is the case, alternative coupling schemes are next examined to identify any differences.

5.3.2   Tree coupling scheme

One possible alternative is a tree-like coupling scheme, with each state coupled to two higher energy states. The specific case considered in this study was for constant coupling strengths of 4 MeV, and the same ladder of energies. This scheme is visualised in Figure **??**.

The state populations do what would be expected for a two level tree, behaving in a similar fashion to the two-channel case discussed previously except sharing the wavefunction density equally between the two channels.

However, this highly regular oscillation remains for higher order couplings. As seen in Figure 5.24, the level populations oscillate slightly slower than the two level case, with the channels in each level are equally populated at all timesteps. One key difference between these two cases is the extension of the time at near zero population for the entrance channel.
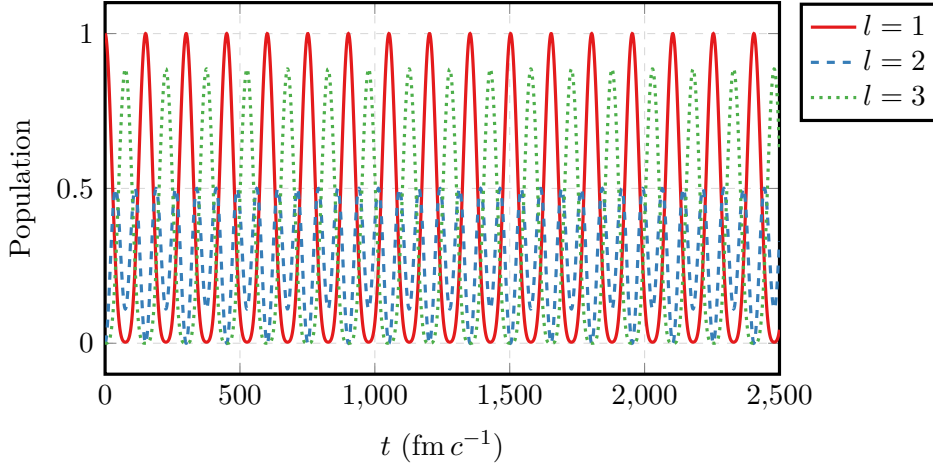
Figure 5.24: Level populations overtime for a three level tree.

Another is a change in the period, which increased from approximately 110 to 150 $\mathrm{fm}\,c^{-1}$. Testing higher levelled cases of the tree scheme would shed light on whether this period continues to increase along with the widening at near zero entrance channel population. Over these simulations the speed of Quantum Toolbox was seen to be consistently linear with the number of channels. Doubling of the number of channels per level means a large tree configuration would require orders of magnitude more time than the three level case. This is beyond the scope of this thesis, but is a promising path to follow in the future.

Even referencing just two and three level examples, it appears that the observed extension of unpopulated time in the entrance channel appears to be due to the matching phases of the couplings, as opposed to a mismatching. While the previous simulations show promising slow oscillations in the entrance channel population, both for the "ladder" and "tree" coupling schemes, further coupling schemes may show even stronger slow oscillatory behaviour. Subsequent studies were done on complete coupling systems, with couplings between every pair of states, to remove any structural symmetry in the coupling scheme.

5.3.3 Complete coupling schemes

Another alternative is a complete coupling scheme, where all channels in the linear "ladder" scheme (Figure **??**) are connected to all others. To remove the potential dependence on symmetries in the coupling strength two forms of this were examined; complete coupling with equal strength couplings, and with random couplings. The equal strength couplings were chosen to be 4 MeV to match previous computations, and the random couplings were chosen uniformly between 0 and 4 MeV.
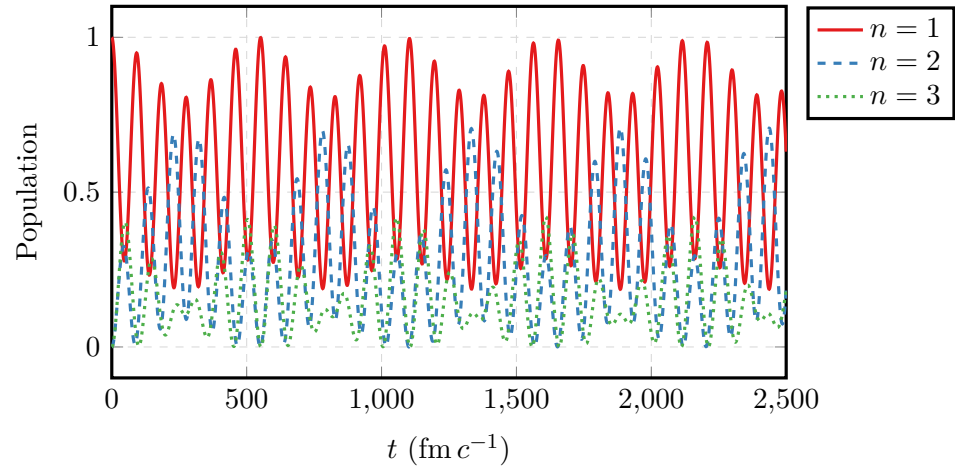
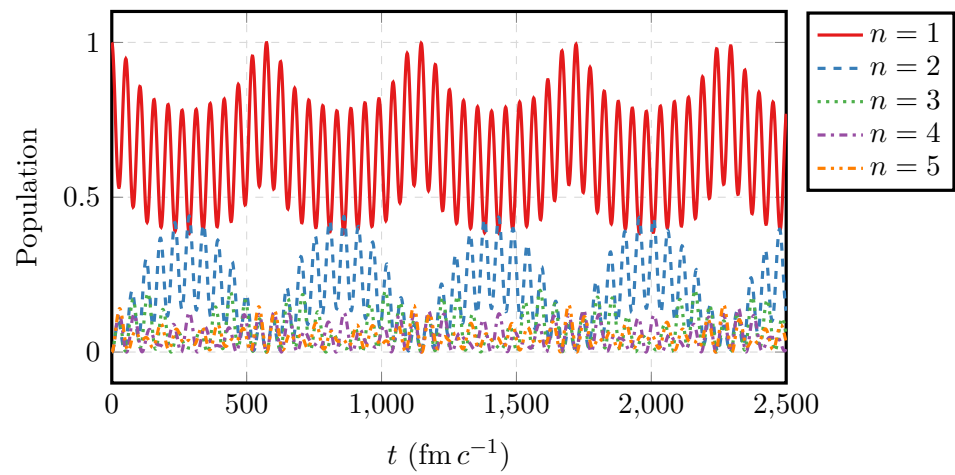Figure 5.25: Channel populations overtime for three equally coupled states.

Figure 5.26: Channel populations overtime for five equally coupled states.
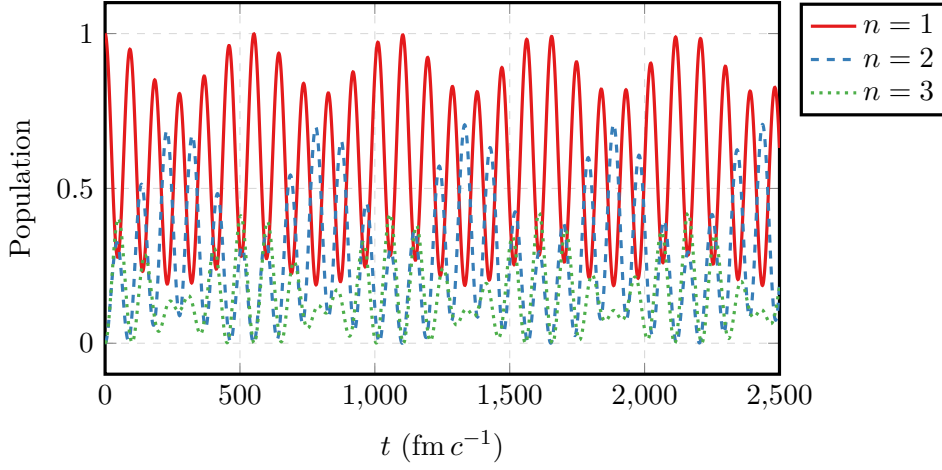
Figure 5.27: Channel populations overtime for three randomly coupled states.

The randomly chosen couplings for three channels were

$$
V_3 = \begin{bmatrix} V_0 & 3.4 & 1.6 \\ 3.4 & V_0 & 3.1 \\ 1.6 & 3.1 & V_0 \end{bmatrix}
\tag{5.2}
$$

The randomly chosen couplings for five channels were

$$
V_5 = \begin{bmatrix} V_0 & 3.6 & 1.3 & 2.2 & 3.7 \\ 3.6 & V_0 & 1.1 & 1.5 & 2.5 \\ 1.3 & 1.1 & V_0 & 2.1 & 2.9 \\ 2.2 & 1.5 & 2.1 & V_0 & 0.6 \\ 3.7 & 2.5 & 2.9 & 0.6 & V_0 \end{bmatrix}
\tag{5.3}
$$

5.3.4 Evidence of recurring ground state dissipation

There appear to be two opposite possibilities when it comes to depleting the ground state of flux for a sustained period of time. Perhaps the most intuitive is a random complete coupling scheme which lacks structure in the couplings and their strengths. As the coupling strength is effectively the "rate" wavefunction density is moved between channels, the cumulative contribution of the channels needs to synchronise to see recurrence. If the channels lack symmetries then the lowest common multiple of the numbers is on average
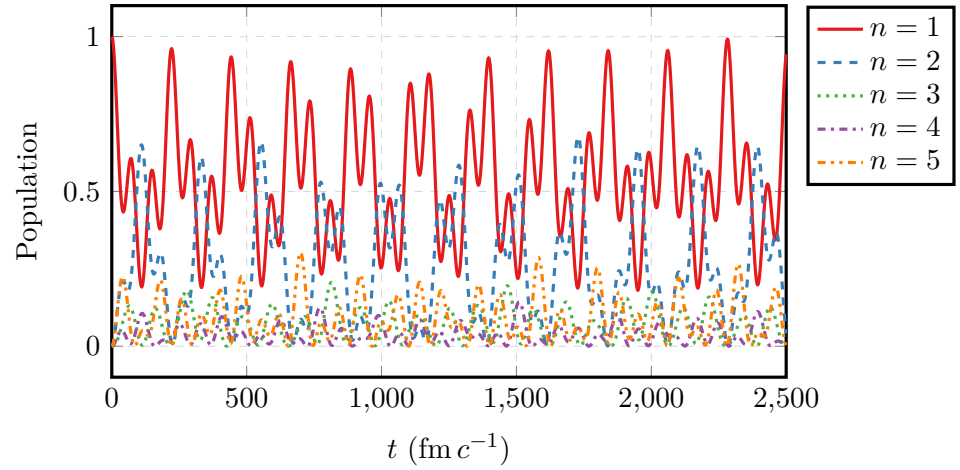
Figure 5.28: Channel populations overtime for five randomly coupled states.

larger, and the recurrence time must be longer.

Surprisingly, there is some indication that having an extremely symmetric system such as the "tree" coupling scheme has the property of extending recurrence time with the number of channels. Intuitively, this appears related to the small number of paths that connect flux into the entrance channel relative to others. In any channel, two out of three channels move flux away from the entrance channel. Further studies can reveal whether this is a correct assumption.

Conclusion

Even after creating 24 synthetic elements and many more isotopes, the dissipative processes that underlie all fusion are still poorly understood. Calculations in nuclear reaction dynamics employ static coupled channels approaches to estimate the probability that the nuclei pass the barrier and interact strongly. A systematic over-prediction of the barrier passing rate by static coupled channels is attributable to neglect of dissipative effects before interaction with the barrier, which in practice can only be included by time-dependent calculations. Time-dependent methods open up the possibility of also describing the highly dissipative physics of fusion itself.

This thesis has presented a new application of the time-dependent coupled channels approach to nuclear collisions, to include uniquely time-dependent dissipative effects in fusion. A split-step Fourier method on spacial and conjugate grids was presented, allowing sets of coupled time-dependent Schrödinger equations to be solved. This method was implemented as part of a flexible C++ library, Quantum Toolbox, which can solve time-dependent coupled channels equations in time linear to the number of channels. Employing wavepackets, the code was shown in Chapter 4 to match both analytic transmissions from tunnelling and static coupled channels solutions.

The code was then applied to two open problems; suppression of above barrier transmission due to dissipation, and time-dependent fusion as trapping resulting from dissipation into higher order couplings. Several promising results have provided insight into these problems.

Approximating the form of the barrier by a Gaussian, the strength and location of the couplings were varied to investigate the effect on barrier transmission. For the above barrier suppression, allowing the channels to couple earlier in the reaction by shifting the coupling potential forward matched the qualitative form of the above and below barrier transmission seen for heavy elements. This indicates that coupling in this region is the mechanism for high energy hindrance, reducing the mean energy and thus the transmission

above the barrier.

Studies of wavefunction trapping inside the barrier presented two clear paths to longer term dissipation in the ground state; highly symmetric coupling schemes, and highly asymmetric coupling schemes. Both of these schemes presented a significant reduction in the entrance channel population for a significant amount of time compared to typical nuclear collision zeptosecond timescales. This shows promise as a technique for simulating fusion without the need for artificial boundary conditions or absorbing potentials.

6.1 Limits of time-dependent coupled channels

The limits of time-dependent coupled channels are generally also limitations with static coupled channels, and we briefly summarise them here, along with avenues for mitigation of these limitations.

The most significant limit of coupled channels is the phenomenological form of the couplings, the states and the energies. Many of the energies and states can in general be known from nuclear structure theory and Hartree-Fock methods, but the form of the couplings still poses a problem. This makes confirmation of the chosen forms difficult also, since matching experimental results doesn't necessitate that the given configuration is correct. There may be many seemingly unrelated configurations that result in the same macroscopic transmission and reflection curves.

However, using mean field methods such as Hartree-Fock to produce several of the important factors, including the form of the nuclear potential and the important low-lying excited states of the ions can improve confidence in the coupled channels results [19]. Constraining the coupled channel forms further with techniques such as the WKB and no-Coriolis approximations from path integral formalism can also provide information on these states. In the future, computers may even improve enough that lattice QCD can improve on the Hartree-Fock nuclear form [28, 67, 68]. This constraining of states reduces the possibility for model error in time-dependent coupled channels calculations.

Another issue with coupled channels methods, and particularly time-dependent coupled channels, is their approximate form. It is impossible to include every single possible reaction channel in the equations, as they become unbound and continuous for high energies. The number of states are limited for computational efficiency, a more significant problem for time-dependent coupled channels as more computations are required for propagation than solving the static eigensystem.

The current time-dependent coupled channels approach does not appear to easily allow for dissipation of angular momentum. In general the quantum angular momentum of relative motion L is conserved, as nuclear reactions are closed systems. This may be important for later stage capture processes as the compound nucleus forms, but may not necessarily contribute in the dissipative early stages. This is a significant factor to consider for any future work using time-dependent coupled channels.

6.2   Future directions

While some preliminary conclusions have been reached regarding the treatment of dissipation and fusion, there is much work that remains to be done. Firstly, a more thorough survey of coupling schemes needs to be performed, to fully understand the relationship between the input parameters and the resulting observables including the transmission, the reflection and the barrier distributions on a by-channel basis. A similar survey is needed in a trapping potential, to understand exactly what realistically allows for removal of the ground state wavefunction to higher order states.

Clear candidates for sources of observed dissipation were identified for both cases. In the case of pre-fusion dissipation, early coupling requires more in depth study to confirm whether it is the correct description of this phenomenon and to compare with experiment. Combining a coupling on the forward edge of the barrier with another in the interior would be a better match for real reactions and their possible states. Testing to see if this coupling form can produce similar transmission curves to the forward shifted potential would provide further evidence supporting this form of coupling as a contributor to dissipation.

In the case of fusion through coupling into higher energy states in the nuclear overlap region inside the barrier, many possibilities still exist. Both highly symmetric and highly asymmetric coupling scheme data indicated some form of entrance channel dissipation. Investigation of many channel coupling schemes for the symmetric "tree" and asymmetric complete random coupling schemes would confirm whether this behaviour continues to increase for more channels. Further possibilities to reduce the symmetry include randomly stepping the internal channel energies, and incrementing prime number coupling strengths or energies.

Measurements of fusion cross sections for very weakly bound light nuclei, where dissipation would be expected to occur early in the collision might be of interest for testing these ideas further [69]. An example of such a system is ^{12}C+^{20}C.

While there is a positive outlook on the future use of time-dependent coupled channels to account for dissipation in and before fusion, there are many more varied uses of a time-dependent code applied to the same problems as static coupled channels. Understanding variations over the time of a reaction allow further probing of nuclear reactions. Further, with a concrete description of important states and couplings, the time-dependence of quasi-elastic and capture reactions could potentially be matched to the lifetimes of the simulated nuclei, to estimate the component reaction products for a given system.

If the time-dependent coupled channels method becomes as widely used as current coupled channels codes, such as CCFULL, it will be worthwhile to improve the code enough to see widespread use. There are many different aspects of the code that can be improved, including speed and accuracy.

The possible first steps to improve calculation speed include CPU-based optimisation, for which Intel's MKL can be used instead of Eigen for optimised basic vector and matrix operations on Intel CPUs [70]. Intel MKL is proven to be very fast for operations on matrices, and has efficient algorithms for all operations performed in Quantum Toolbox currently. This includes the Fast Fourier Transformation, for which Intel MKL has been shown to outperform FFTW, which is currently used in Quantum Toolbox [65]. To squeeze the most performance out of the code, careful parallelisation of machine code is even possible to dramatically speed up Fourier transformation-based propagation [71].

There are also several ways to improve accuracy. The most obvious choices are to evaluate higher order splitting methods to reduce the error contribution from the timestep, allowing larger steps to be taken. Alternative methods of applying the kinetic operator can also be evaluated for nuclear physical problems, to ensure that the best solution is being used for the nuclear context.

6.3   Outlook

The above limitations considered, there are many ways in which time dependent coupled channels can contribute to an improved understanding of heavy ion fusion. The future of time-dependent coupled channels is bright, with many interesting problems worth probing time-dependently. Through a mix of macroscopic theory such as this, and further developments in structure and low energy QCD, there may be a time on the horizon when the dynamics leading to fusion are understood, and the "island of stability" comes into view.

Solving static couplings using the Numerov algorithm

Expansion of wavefunctions in the eigenbasis of the internal Hamiltonian leads to a system of n coupled ordinary differential equations. For small systems, for example $n = 2$, it may be possible to apply a transformation, decoupling the equations and allowing them to be solved separately. However, in higher dimensional systems this is not generally possible. In these cases, the system of equations needs to be solved numerically. An algorithm which is often employed for this purpose, due to its ease of use, is the Numerov algorithm.

In this chapter I present a derivation of the Numerov algorithm, demonstrating its accuracy and reasonable computational cost. After this, the exact use of the Numerov algorithm in systems of coupled equations is shown.

A.1   Derivation of the Numerov algorithm

Authors note: This derivation has been based on that shown in [72].

The Numerov algorithm can be applied to any second order ordinary differential equations without a first order term. These have the form:

$$\frac{\mathrm{d}^2}{\mathrm{d}x^2}\psi(x) = -g(x)\psi(x) + s(x) \tag{A.1}$$

If the function $\psi(x)$ is discretised on a grid with step size h, adjacent points on the grid can be approximated by a Taylor expansion

$$\begin{aligned}
\psi(x + h) = {} & \psi(x) + h\frac{\mathrm{d}}{\mathrm{d}x}\psi(x) + \frac{h^2}{2}\frac{\mathrm{d}^2}{\mathrm{d}x^2}\psi(x) + \frac{h^3}{6}\frac{\mathrm{d}^3}{\mathrm{d}x^3}\psi(x) + \frac{h^4}{24}\frac{\mathrm{d}^4}{\mathrm{d}x^4}\psi(x) \\
& + \frac{h^5}{120}\frac{\mathrm{d}^5}{\mathrm{d}x^5}\psi(x) + \mathcal{O}(h^6)
\end{aligned} \tag{A.2}$$

and

$$\psi(x - h) = \psi(x) - h\frac{\mathrm{d}}{\mathrm{d}x}\psi(x) + \frac{h^2}{2}\frac{\mathrm{d}^2}{\mathrm{d}x^2}\psi(x) - \frac{h^3}{6}\frac{\mathrm{d}^3}{\mathrm{d}x^3}\psi(x) + \frac{h^4}{24}\frac{\mathrm{d}^4}{\mathrm{d}x^4}\psi(x)$$
$$- \frac{h^5}{120}\frac{\mathrm{d}^5}{\mathrm{d}x^5}\psi(x) + \mathcal{O}(h^6) \tag{A.3}$$

Adding these two equations removes the odd terms, giving the expression

$$\psi(x + h) + \psi(x - h) = 2\psi(x) + h^2\frac{\mathrm{d}^2}{\mathrm{d}x^2}\psi(x) + \frac{h^4}{12}\frac{\mathrm{d}^4}{\mathrm{d}x^4}\psi(x) + \mathcal{O}(h^6) \tag{A.4}$$

Rearranging gives an expression for $\dfrac{\mathrm{d}^2}{\mathrm{d}x^2}\psi(x)$,

$$\frac{\mathrm{d}^2}{\mathrm{d}x^2}\psi(x) = \frac{1}{h^2}\left(\psi(x + h) - 2\psi(x) + \psi(x - h)\right) - \frac{h^2}{12}\frac{\mathrm{d}^4}{\mathrm{d}x^4}\psi(x) + \mathcal{O}(h^4) \tag{A.5}$$

A simple expression without the fourth order term is desirable, and a form can be found for this by differentiating the original ODE, Equation A.1, twice with respect to x. This gives

$$\frac{\mathrm{d}^4}{\mathrm{d}x^4}\psi(x) = \frac{\mathrm{d}^2}{\mathrm{d}x^2}\left(-g(x)\psi(x) + s(x)\right)$$
$$= -\frac{\mathrm{d}^2}{\mathrm{d}x^2}\left(g(x)\psi(x)\right) + \frac{\mathrm{d}^2}{\mathrm{d}x^2}s(x) \tag{A.6}$$

In the same way as for ψ, these second order terms can be approximated by Taylor expansion as

$$\frac{\mathrm{d}^2}{\mathrm{d}x^2}\left(g(x)\psi(x)\right) = \frac{1}{h^2}\left(g(x + h)\psi(x + h) - 2g(x)\psi(x) + g(x - h)\psi(x - h)\right)$$
$$+ \mathcal{O}(h^2) \tag{A.7}$$

and
$$\frac{\mathrm{d}^2}{\mathrm{d}x^2}s(x) = \frac{1}{h^2}\left(s(x + h) - 2s(x) + s(x - h)\right) + \mathcal{O}(h^2) \tag{A.8}$$

Substituting these approximations back into Equation A.6 gives

$$\frac{\mathrm{d}^4}{\mathrm{d}x^4}\psi(x) = -\frac{1}{h^2}\left(g(x + h)\psi(x + h) - 2g(x)\psi(x) + g(x - h)\psi(x - h)\right)$$
$$+ \frac{1}{h^2}\left(s(x + h) - 2s(x) + s(x - h)\right) + \mathcal{O}(h^2) \tag{A.9}$$

Substituting into Equation A.5 gives

$$\frac{d^2}{dx^2}\psi(x) = \frac{1}{h^2}\left(\psi(x+h) - 2\psi(x) + \psi(x-h)\right)$$
$$+ \frac{1}{12}\left(g(x+h)\psi(x+h) - 2g(x)\psi(x) + g(x-h)\psi(x-h)\right) \quad \text{(A.10)}$$
$$- \frac{1}{12}\left(s(x+h) - 2s(x) + s(x-h)\right) + \mathcal{O}(h^4)$$

To obtain the final Numerov equation, the $\frac{d^2}{dx^2}\psi(x)$ term is substituted for $-g(x)\psi(x) + s(x)$, and the terms rearranged

$$-g(x)\psi(x) + s(x) = \frac{1}{h^2}\left(\psi(x+h) - 2\psi(x) + \psi(x-h)\right)$$
$$+ \frac{1}{12}\left(g(x+h)\psi(x+h) - 2g(x)\psi(x) + g(x-h)\psi(x-h)\right)$$
$$- \frac{1}{12}\left(s(x+h) - 2s(x) + s(x-h)\right) + \mathcal{O}(h^4)$$
$$0 = \psi(x+h)\left(1 + \frac{h^2}{12}g(x+h)\right) - 2\psi(x)\left(1 - \frac{5h^2}{12}g(x)\right) \quad \text{(A.11)}$$
$$+ \psi(x-h)\left(1 + \frac{h^2}{12}g(x-h)\right)$$
$$- \frac{h^2}{12}\left(s(x+h) + 10s(x) + s(x-h)\right) + \mathcal{O}(h^4)$$

In practice, it is simpler to view these functions as defined on a grid of step size h. In this way, the point $\psi(x)$ can be relabelled ψ_n, and similarly $\psi(x+h)$ to ψ_{n+1}. In this way, the Numerov equation can be rewritten as

$$\psi_{n+1}\left(1 + \frac{h^2}{12}g_{n+1}\right) \approx -2\psi_n\left(1 - \frac{5h^2}{12}g_n\right) + \psi_{n-1}\left(1 + \frac{h^2}{12}g_{n-1}\right)$$
$$- \frac{h^2}{12}\left(s_{n+1} + 10s_n + s_{n-1}\right) + \mathcal{O}(h^4) \quad \text{(A.12)}$$

or explicitly the expression for ψ_{n+1} in terms of ψ_n and ψ_{n-1}

$$\psi_{n+1} \approx \frac{1}{\left(1 + \frac{h^2}{12}g_{n+1}\right)}\left(-2\psi_n\left(1 - \frac{5h^2}{12}g_n\right) + \psi_{n-1}\left(1 + \frac{h^2}{12}g_{n-1}\right)\right)$$
$$- \frac{h^2}{12\left(1 + \frac{h^2}{12}g_{n+1}\right)}\left(s_{n+1} + 10s_n + s_{n-1}\right) + \mathcal{O}(h^4) \quad \text{(A.13)}$$

So given the first two points of a function ψ on a grid, each subsequent point can be quickly calculated to reasonable accuracy using this iterative equation.

A.2 Solving coupled systems of equations

Explanation of implementation to coupled system of equations.

In some cases, including the coupled channels formalism, a system of Numerov-type differential equations may need to be solved. In the case of coupled channels, the system of N equations takes the form

$$\frac{\mathrm{d}^2}{\mathrm{d}x^2}\psi_i(x) = -g(x)\psi_i(x) + s_i(x) \tag{A.14}$$

where $s_i(x) = \sum_{n\neq i} c_n(x)\psi_n(x)$. Before, the goal was to approximate a single function with a single iterative scheme. Now, the $s_i(x)$ for each equation is itself composed of unknown functions. This may seem to pose a problem, as how could you expect to find a good approximation to the functions if your inputs are incorrect? Thankfully, it can be shown empirically that using another iteration scheme resolves this issue.

The iteration scheme is simple, following a process familiar to those in computational mathematics. Starting with some initial guess ψ_i^0 for each ψ_i, Algorithm 2 is followed.

Algorithm 2 Coupled Numerov Algorithm

---
for $i \in \{1,\ldots,N\}$ **do**
　　$\psi_i^1 \leftarrow \mathrm{Num}_i$　　　　　　　　　　　　　　　$\triangleright$ Calculate ψ_i^1 using Numerov
end for
$n \leftarrow 1$
while $\sum_{i=1}^{N} \left|\psi_i^n - \psi_i^{n-1}\right| <$ tolerance **do**　　$\triangleright$ Stop when subsequent changes are small
　　for $i \in \{1,\ldots,N\}$ **do**
　　　　$\psi_i^{n+1} \leftarrow \mathrm{Num}_i$　　　　　　　　　　$\triangleright$ Calculate ψ_i^{n+1} using Numerov
　　end for
end while

Qualitatively, this algorithm updates the guess for each ψ_i given the most recent guesses for all ψ_i. This is repeated for each until the updates are within some tolerance of the previous iteration. In practice wavefunctions are usually "nice" mathematical objects, and so the algorithm easily converges. Therefore a tiny tolerance can be chosen, with confidence that the Coupled Numerov Algorithm will eventually converge.

While there is no formal proof that this procedure is always convergent given a starting guess, this algorithm has been shown to work well for decades in solving coupled channels problems. No convergence issues were found with the algorithm for any case considered in this thesis.

C++ Code: Quantum Toolbox

The Quantum Toolbox is publicly available without technical support at `https://github.com/EmlynG/QuantumToolbox`. The code will continue to see updates as it is used for new problems in nuclear dynamics, and may be moved from this location. If the above link is no longer active, please contact me, Emlyn Graham (emlyn.graham@anu.edu.au) or my supervisor, Dr. Edward Simpson (edward.simpson@anu.edu.au) for more information.

Bibliography

[1] Christian Iliadis. *Nuclear Physics of Stars*. 2015. ISBN 9783527406029. doi: 10. 1002/9783527618750.

[2] J. R. Leigh, M. Dasgupta, D. J. Hinde, J. C. Mein, C. R. Morton, R. C. Lemmon, J. P. Lestone, J. O. Newton, H. Timmers, J. X. Wei, and N. Rowley. Barrier distributions from the fusion of oxygen ions with Sm144,148,154 and W186. *Physical Review C*, 1995. ISSN 05562813. doi: 10.1103/PhysRevC.52.3151.

[3] C. H. Dasso, S. Landowne, and A. Winther. Channel-coupling effects in heavy-ion fusion reactions. *Nuclear Physics, Section A*, 1983. ISSN 03759474. doi: 10.1016/ 0375-9474(83)90578-X.

[4] K. Hagino, N. Rowley, and A.T. T. Kruppa. A program for coupled-channel calculations with all order couplings for heavy-ion fusion reactions. *Computer Physics Communications*, 1999. ISSN 00104655. doi: 10.1016/s0010-4655(99)00243-x.

[5] J. O. Newton, R. D. Butt, M. Dasgupta, D. J. Hinde, I. I. Gontchar, C. R. Morton, and K. Hagino. Systematic failure of the Woods-Saxon nuclear potential to describe both fusion and elastic scattering: Possible need for a new dynamical approach to fusion. *Physical Review C - Nuclear Physics*, 2004. ISSN 05562813. doi: 10.1103/ PhysRevC.70.024605.

[6] Yu Ts Oganessian, V K Utyonkov, YuV Lobanov, and A N Other. Synthesis of the isotopes of elements 118 and 116 in the 249Cf and 245Cm + 48Ca fusion reactions. *Physical Review C*, 2006.

[7] John David Jackson. Classical Electrodynamics Third Edition. *American Journal of Physics*, 1999. ISSN 9780471309321.

[8] Ian J. Thompson and Filomena M. Nunes. *Nuclear Reactions for Astrophysics*. 2009. doi: 10.1017/cbo9781139152150.

[9] E. Rutherford. LXXIX. The scattering of α and β particles by matter and the structure of the atom. *The London, Edinburgh, and Dublin Philosophical Magazine and Journal of Science*, 1911. ISSN 1941-5982. doi: 10.1080/14786440508637080.

[10] J. Toke, R. Bock, G. X. Dai, A. Gobbi, S. Gralla, K. D. Hildenbrand, J. Kuzminski, W. F.J. Müller, A. Olmi, H. Stelzer, B. B. Back, and S. Bjørnholm. Quasi-fission - The mass-drift mode in heavy-ion reactions. *Nuclear Physics, Section A*, 1985. ISSN 03759474. doi: 10.1016/0375-9474(85)90344-6.

[11] Luciano G. Moretto. The phenomenology of deep-inelastic processes. 409, 1983.

[12] Niels Bohr. Neutron capture and nuclear constitution. *Niels Bohr Collected Works*, 137(3461):151–156, 1986. ISSN 18760503. doi: 10.1016/S1876-0503(08)70464-X.

[13] Walter Loveland. Characterizing the mechanism(s) of heavy element synthesis reactions. In *EPJ Web of Conferences*, 2016. ISBN 9782759890118. doi: 10.1051/epjconf/201613104003.

[14] C. Simenel, D. J. Hinde, R. du Rietz, M. Dasgupta, M. Evers, C. J. Lin, D. H. Luong, and A. Wakhle. Influence of entrance-channel magicity and isospin on quasi-fission. *Physics Letters, Section B: Nuclear, Elementary Particle and High-Energy Physics*, 2012. ISSN 03702693. doi: 10.1016/j.physletb.2012.03.063.

[15] G. Mohanto, D. J. Hinde, K. Banerjee, M. Dasgupta, D. Y. Jeung, C. Simenel, E. C. Simpson, A. Wakhle, E. Williams, I. P. Carter, K. J. Cook, D. H. Luong, C. S. Palshetkar, and D. C. Rafferty. Interplay of spherical closed shells and N/Z asymmetry in quasifission dynamics. *Physical Review C*, 97(5):1–10, 2018. ISSN 24699993. doi: 10.1103/PhysRevC.97.054603.

[16] David J. Rowe. *Nuclear collective motion: Models and theory.* 2010. ISBN 9789812790668. doi: 10.1142/6721.

[17] A. Montina. Exponential complexity and ontological theories of quantum mechanics. *Physical Review A - Atomic, Molecular, and Optical Physics*, 77(2):1–11, 2008. ISSN 10502947. doi: 10.1103/PhysRevA.77.022104.

[18] J. W. Negele. The mean-field theory of nuclear structure and dynamics. *Reviews of Modern Physics*, 1982. ISSN 00346861. doi: 10.1103/RevModPhys.54.913.

[19] C. Simenel, M. Dasgupta, D. J. Hinde, and E. Williams. Microscopic approach to coupled-channels effects on fusion. *Physical Review C - Nuclear Physics*, 88(6):1–15, 2013. ISSN 1089490X. doi: 10.1103/PhysRevC.88.064604.

[20] Jeff Greensite. An Introduction to the Confinement Problem. *An Introduction to the Confinement Problem*, 2011. ISSN 0028-0836. doi: 10.1007/978-3-642-14382-3.

[21] David J. Gross and Frank Wilczek. Ultraviolet behavior of non-abelian gauge theories. *Physical Review Letters*, 1973. ISSN 00319007. doi: 10.1103/PhysRevLett.30.1343.

[22] H. David Politzer. Reliable perturbative results for strong interactions? *Physical Review Letters*, 1973. ISSN 00319007. doi: 10.1103/PhysRevLett.30.1346.

[23] J. R. Stone and P. G. Reinhard. The Skyrme interaction in finite nuclei and nuclear matter, 2007. ISSN 01466410.

[24] R. P. Feynman and A. R. Hibbs. *Quantum mechanics and path integrals.* McGraw-Hill, New York, 1965.

[25] A. B. Balantekin and N. Takigawa. Path integral approach to multidimensional quantum tunnelling. *Annals of Physics*, 1985. ISSN 1096035X. doi: 10.1016/0003-4916(85) 90152-6.

[26] A. B. Balantekin and N. Takigawa. Quantum tunneling in nuclear fusion. *Reviews of Modern Physics*, 1998. ISSN 0034-6861. doi: 10.1103/revmodphys.70.77.

[27] D. M. Brink and U. Smilansky. Multiple reflections in the path-integral approach to barrier penetration. *Nuclear Physics, Section A*, 1983. ISSN 03759474. doi: 10.1016/0375-9474(83)90574-2.

[28] K. Hagino, N. Takigawa, A. B. Balantekin, and J. R. Bennett. Path integral approach to no-Coriolis approximation in heavy-ion collisions. *Physical Review C*, 1995. ISSN 05562813. doi: 10.1103/PhysRevC.52.286.

[29] Roger D. Woods and David S. Saxon. Diffuse surface optical model for nucleon-nuclei scattering [19], 1954. ISSN 0031899X.

[30] Kouichi Hagino. *Multi-dimensional Quantum Tunneling in Heavy-Ion Fusion Reactions.* PhD thesis, 1998.

[31] G. R. Satchler. Heavy-ion scattering and reactions near the Coulomb barrier and "threshold anomalies", 1991. ISSN 03701573.

[32] Y. Eisen and Z. Vager. The incoming wave boundary condition for elastic scattering of heavy particles at incident energies near the coulomb barrier. *Nuclear Physics, Section A*, 1972. ISSN 03759474. doi: 10.1016/0375-9474(72)90085-1.

[33] M. Dasgupta, D. J. Hinde, A. Diaz-Torres, B. Bouriquet, Catherine I. Low, G. J. Milburn, and J. O. Newton. Beyond the coherent coupled channels description of nuclear fusion. *Physical Review Letters*, 2007. ISSN 00319007. doi: 10.1103/PhysRevLett.99. 192701.

[34] D. J. Hinde, M. Dasgupta, A. Diaz-Torres, and M. Evers. Quantum coherence and decoherence in low energy nuclear collisions: from superposition to irreversibility. *Nuclear Physics A*, 2010. ISSN 03759474. doi: 10.1016/j.nuclphysa.2009.12.019.

[35] Alexis Diaz-Torres. Coupled-channels density-matrix approach to low-energy nuclear reaction dynamics. In *AIP Conference Proceedings*, 2011. ISBN 9780735409378. doi: 10.1063/1.3628370.

[36] Nobuhiro Yamanaka and Yasushi Kino. Time-dependent coupled-channel calculations of positronium-formation cross sections in positron-hydrogen collisions. *Physical Review A - Atomic, Molecular, and Optical Physics*, 2001. ISSN 10941622. doi: 10.1103/PhysRevA.64.042715.

[37] M. Tokieda and K. Hagino. Quantum tunneling with friction. *Physical Review C*, 2017. ISSN 24699993. doi: 10.1103/PhysRevC.95.054604.

[38] Terence Vockerodt and Alexis Diaz-Torres. Describing heavy-ion fusion with quantum coupled-channels wave-packet dynamics. *Physical Review C*, 100(3):1–6, 2019. ISSN 2469-9985. doi: 10.1103/physrevc.100.034606.

[39] J. C. Light, I. P. Hamilton, and J. V. Lill. Generalized discrete variable approximation in quantum mechanics. *The Journal of Chemical Physics*, 1985. ISSN 00219606. doi: 10.1063/1.448462.

[40] G. W. Richings, I. Polyak, K. E. Spinlove, G. A. Worth, I. Burghardt, and B. Lasorne. Quantum dynamics simulations using Gaussian wavepackets: the vMCG method. *International Reviews in Physical Chemistry*, 34(2):269–308, 2015. ISSN

1366591X. doi: 10.1080/0144235X.2015.1051354. URL http://dx.doi.org/10.1080/0144235X.2015.1051354.

[41] Liang You Peng and Anthony F. Starace. Application of Coulomb wave function discrete variable representation to atomic systems in strong laser fields. *Journal of Chemical Physics*, 2006. ISSN 00219606. doi: 10.1063/1.2358351.

[42] Arieh Iserles and Karolina Kropielnicka. Effective approximation for linear time-dependent Schrödinger equation. 2011.

[43] Gilbert Strang. On the Construction and Comparison of Difference Schemes. *SIAM Journal on Numerical Analysis*, 1968. ISSN 0036-1429. doi: 10.1137/0705041.

[44] Benedict Leimkuhler and Sebastian Reich. *Simulating Hamiltonian Dynamics*. 2005. doi: 10.1017/cbo9780511614118.

[45] André D. Bandrauk and Hai Shen. Improved exponential split operator method for solving the time-dependent Schrödinger equation. *Chemical Physics Letters*, 1991. ISSN 00092614. doi: 10.1016/0009-2614(91)90232-X.

[46] André D. Bandrauk, Effat Dehghanian, and Huizhong Lu. Complex integration steps in decomposition of quantum exponential evolution operators. *Chemical Physics Letters*, 2006. ISSN 00092614. doi: 10.1016/j.cplett.2005.12.006.

[47] C. Cohen-Tannoudji, B. Diu, and F. Laloe. *Quantum Mechanics*. 1991. ISBN 1848729197. doi: 10.4324/9780203080719.ch9. URL https://www.taylorfrancis.com/books/9780203080719.

[48] J. J. Sakurai. Modern Quantum Mechanics Revised Edition, 1994.

[49] C. Lanczos. An iteration method for the solution of the eigenvalue problem of linear differential and integral operators. *Journal of Research of the National Bureau of Standards*, 1950. ISSN 0091-635. doi: 10.6028/jres.045.026.

[50] J. G. F. Francis. The QR Transformation A Unitary Analogue to the LR Transformation–Part 1. *The Computer Journal*, 1961. ISSN 0010-4620. doi: 10.1093/comjnl/4.3.265.

[51] J. G. F. Francis. The QR Transformation–Part 2. *The Computer Journal*, 1962. ISSN 0010-4620. doi: 10.1093/comjnl/4.4.332.

[52] V. N. Kublanovskaya. On some algorithms for the solution of the complete eigenvalue problem. *USSR Computational Mathematics and Mathematical Physics*, 1962. ISSN 00415553. doi: 10.1016/0041-5553(63)90168-X.

[53] J. J.M. Cuppen. A divide and conquer method for the symmetric tridiagonal eigenproblem. *Numerische Mathematik*, 1980. ISSN 09453245. doi: 10.1007/BF01396757.

[54] Max Planitz and E. Anderson. LAPACK Users Guide. *The Mathematical Gazette*, 1995. ISSN 00255572. doi: 10.2307/3620088.

[55] Steven G. Johnson and Matteo Frigo. A modified split-radix FFT with fewer arithmetic operations. *IEEE Transactions on Signal Processing*, 2007. ISSN 1053587X. doi: 10.1109/TSP.2006.882087.

[56] Thiab R. Taha and Mark I. Ablowitz. Analytical and numerical aspects of certain nonlinear evolution equations. II. Numerical, nonlinear Schrödinger equation. *Journal of Computational Physics*, 1984. ISSN 10902716. doi: 10.1016/0021-9991(84)90003-2.

[57] C. Leforestier, R. H. Bisseling, C. Cerjan, M. D. Feit, R. Friesner, A. Guldberg, A. Hammerich, G. Jolicard, W. Karrlein, H. D. Meyer, N. Lipkin, O. Roncero, and R. Kosloff. A comparison of different propagation schemes for the time dependent Schrödinger equation. *Journal of Computational Physics*, 1991. ISSN 10902716. doi: 10.1016/0021-9991(91)90137-A.

[58] Mamadou Ndong, Hillel Tal-Ezer, Ronnie Kosloff, and Christiane P. Koch. A Chebychev propagator with iterative time ordering for explicitly time-dependent Hamiltonians. *Journal of Chemical Physics*, 2010. ISSN 00219606. doi: 10.1063/1.3312531.

[59] David J. Tannor. *Introduction to Quantum Mechanics: A Time-Dependent Perspective.* University Science Books, Sausalito, 1st edition, 2007.

[60] Wolfgang Pauli, C. P. Enz, Ellen Yorke, and Ivan Kramer. Pauli Lectures on Physics. *Physics Today*, 1973. ISSN 0031-9228. doi: 10.1063/1.3128362.

[61] Nicholas J. Higham. Accuracy and stability of numerical algorithms. In *Accuracy and Stability of Numerical Algorithms*, 2002. ISBN 0898715210.

[62] Daoqi Yang. *C++ and Object-Oriented Numeric Computing for Scientists and Engineers.* 2001. doi: 10.1007/978-1-4613-0189-9.

[63] David Padua. FFTW. In *Encyclopedia of Parallel Computing.* 2011. doi: 10.1007/978-0-387-09766-4_397.

[64] Matteo Frigo and Steven G Johnson. The Fastest Fourier Transform in the West (MIT-LCS-TR-728). *Materials Research*, 1997. ISSN 1053587X. doi: 10.1.1.17.5651.

[65] Matteo Frigo and Steven G. Johnson. benchFFT. URL `http://www.fftw.org/benchfft/`.

[66] M. Dasgupta, D. J. Hinde, J. R. Leigh, and K. Hagino. Barrier distributions as a tool to investigate fusion and fission. *Nuclear Physics A*, 1998. ISSN 03759474. doi: 10.1016/S0375-9474(97)00745-8.

[67] Noriyoshi Ishii. Nuclear forces from lattice QCD. In *AIP Conference Proceedings*, 2011. ISBN 9780735409132. doi: 10.1063/1.3584068.

[68] Raúl A. Briceño, Zohreh Davoudi, and Thomas C. Luu. Nuclear reactions from lattice QCD, 2015. ISSN 13616471.

[69] J. Takahashi, M. Munhoz, E. M. Szanto, N. Carlin, N. Added, A. A.P. Suaide, M. M. de Moura, R. L. Liguori Neto, A. Szanto de Toledo, and L. F. Canto. Is fusion inhibited for weakly bound nuclei? *Physical Review Letters*, 1997. ISSN 10797114. doi: 10.1103/PhysRevLett.78.30.

[70] Intel. Intel ® Math Kernel Library Reference Manual. *Numerical Algorithms*, 2007. doi: 10.1535/itj.1101.03.

[71] Ali Khwaldeh, Amani Tahat, and Jordi Marti. Software refactoring: Solving the time-dependent Schrödinger equation via fast Fourier transforms and parallel programming, 2012. ISSN 18125654.

[72] Timothy Sauer. *Numerical analysis*, volume 31. Pearson Education, Inc., Boston, MA, 2012. ISBN 9780321783677. doi: 10.1016/0378-4754(90)90072-q.